J. Fluid Mech. (1988), *vol.* 196, *pp.* 359–408
Printed in Great Britain

The stability of boundary-layer flow over single- and multi-layer viscoelastic walls

By K. S. YEO

Department of Mechanical and Production Engineering, National University of Singapore, Kent Ridge, Singapore 0511, Republic of Singapore

(Received 19 November 1987)

In this paper, we are concerned with the linear stability of zero pressure-gradient laminar boundary-layer flow over compliant walls which are composed of one or more layers of isotropic viscoelastic materials and backed by a rigid base. Wall compliance supports a whole host of new instabilities in addition to the Tollmien–Schlichting mode of instability, which originally exists even when the wall is rigid. The perturbations in the flow and the compliant wall are coupled at their common interface through the kinematic condition of velocity continuity and the dynamical condition of stress continuity. The disturbance modes in the flow are governed by the Orr–Sommerfeld equation using the locally-parallel flow assumption, and the response of the compliant layers is described using a displacement-stress formalism. The theoretical treatment provides a unified formulation of the stability eigenvalue problem that is applicable to compliant walls having any finite number of uniform layers; inclusive of viscous sublayer. The formulation is well suited to systematic numerical implementation. Results for single- and multi-layer walls are presented. Analyses of the eigenfunctions give an insight into some of the physics involved. Multi-layering gives a measure of control over the stability characteristics of compliant walls not available to single-layer walls. The present study provides evidence which suggests that substantial suppression of disturbance growth may be possible for suitably tailored compliant walls.

1. Introduction

Laminar boundary-layer flows over compliant surfaces are susceptible to a wide variety of instabilities. This proliferation was first recognized by Benjamin (1960) in a marvellous piece of analysis. Benjamin's study was motivated by the reported experimental findings of Kramer (1957, 1960) that dramatic drag reduction for towed underwater streamlined bodies could be achieved by coating the bodies with a viscously-damped compliant coating. A comprehensive review of past and current literature can be found in Carpenter & Garrad (1985) or Yeo (1986).

In the broadest sense, the instabilities that arise from the interaction between the compliant surface and the flow may be classified into two categories. The first of these is the Tollmien–Schlichting instability (TSI) which originally exists even when the wall is rigid. The second category consists of those which are brought into being by the compliant response of the wall. We refer to this latter category as compliance-induced flow instabilities (CIFI). The CIFI are none other than those termed FISI (flow-induced surface instabilities) by Carpenter *et al.* We have chosen a slightly different terminology to emphasize the interest in flow stability and the passive nature of the compliant walls. The Tollmien–Schlichting instability is a viscosity-

induced instability and could not exist if the flow were inviscid. Among the compliance-induced instabilities, three main types may be identified. The first two of these are related to the free-surface wave and static deformation modes of the compliant wall; see Yeo & Dowling (1987). They correspond respectively to the flutter and divergence instabilities in the field of aeroelasticity and have frequently been termed as such. The third type of instability is akin to the Kelvin–Helmholtz instability and occurs when the wall or the surface is so soft that there is no real phase speed c at which it can resist the pressure fluctuations of the flow.

In his 1960 work, Benjamin showed that the TSI is stabilized by wall compliance but destabilized by wall damping. The latter contradicted Kramer's notion of stabilization by 'distributed damping'. The flutter modes have just the opposite characteristics. Benjamin's analysis was extended by Landahl (1962) to a workable numerical scheme for the determination of the eigenvalues based upon the matching of the admittances of the flow and the wall. Besides providing some quantitative confirmation of the results of Benjamin (1960), which were founded on qualitative analyses, Landahl offered an interesting physical explanation for the destabilizing influence of wall dissipation on the TSI. For these instabilities, Landahl observed that the total disturbance energy of the coupled system actually decreases with increase in the disturbance amplitude, and consequently, any non-conservative flow of energy from the system must be accompanied by disturbance growth. This energy argument was subsequently generalized by Benjamin (1963) into a three-fold classification scheme for the instabilities. In this scheme, the instability wave is characterized by the sign of the energy needed to activate or excite the disturbance. The Class A waves, of which the TSI is an important example, are characterized by negative activation energy. Disturbance energy must be extracted from the system to create the waves and for the waves to grow. The Class B instability waves, of which the flutter instability is an example, are those which require positive activation energy. For the Class C instability, of which the well-known Kelvin–Helmholtz instability is a prime candidate, the activation energy is zero or nearly so. The major inferences of the early theoretical studies, rooted largely to a temporal interpretation of stability (real wavenumber α and complex frequency ω), are that for successful stabilization, a compliant wall should have high flexibility and low damping to inhibit the Class A TSI waves. However, the damping must be large enough to suppress the Class B waves, and the compliance must not be so large that the Class C Kelvin–Helmholtz type instability can occur. Between these opposing requirements, effective stabilization of the boundary layer appears difficult to achieve.

In addition to being classified by their origin (TSI or CIFI) or according to Benjamin's energy scheme, the instability waves may be further characterized as convective or absolute following the work of Bers & Briggs (1964) in plasma physics. Bearing in mind that in practice, a disturbance is constituted from the superposition of numerous, possibly innumerable, normal wave modes, the unstable development of the disturbance is said to be convective when none of the unstable constituent modes possess zero group velocity. For such instability, the disturbance amplitude at any fixed point in the flow remains small although the disturbance packet may grow as it propagates. There is, however, absolute instability when there exist unstable mode/s having zero group velocity. When this happens constructive interference among modes neighbouring those with zero group velocity occurs leading to the exponential temporal growth of the disturbance at some point in the flow.

The convective nature of boundary-layer flow over a rigid flat plate was emphasized and demonstrated theoretically by Gaster (1965). Such instabilities are somewhat physically better modelled by the use of spatial normal modes (real frequency ω and complex wavenumber α); see Drazin & Reid (1981). The use of spatial modes for modelling convective instability was advocated by Gaster (1965) and was also implied by the theoretical treatment of Bers & Briggs (1964). Instability modes in boundary-layer flow over compliant walls/surfaces are believed to be predominantly convective although the possible occurrence of true absolute instability cannot be excluded in very soft walls; the classical Kelvin–Helmholtz instability is an absolute instability. An example of possible Class A absolute instability was suggested by Carpenter & Garrad (1986) for potential flow over a damped spring-backed bending plate. Absolute instability is a devastating form of instability and very little is known at this time concerning its possible existence in boundary-layer flow over compliant walls. However, even in the very soft walls for which its existence is a possibility, it is more than likely that strong convective-type instabilities will precede the onset of any absolute instability. The establishment of the existence or otherwise of absolute instability in boundary-layer flow over compliant walls is a difficult problem (see Yeo 1986) and will not be addressed in this paper.

In the absence of absolute instability, a temporal interpretation of boundary-layer instability (such as those of the early studies) appears to be overly severe. Given a generally convective nature of boundary-layer instability, reduction in drag via stabilization probably arises as a result of reduced downstream disturbance growth which in turn leads to a delay in the onset of strong nonlinear processes preceding a breakdown to turbulence. The downstream growth of disturbances in boundary-layer flow over compliant membrane was briefly investigated by Landahl & Kaplan (1965). The downstream growth rates were estimated from temporal eigenvalue data using Gaster's relation (Gaster 1962) $\alpha_i \approx -\omega_i/c_g$, where $c_g = \partial\omega_r/\partial\alpha$ is the real group velocity and the subscripts i and r denote respectively the imaginary and real parts of the quantity. Reduced growth was reported for TSI over corresponding rigid wall results. The effect of reduced spatial growth on transition for flows over compliant membrane surfaces was investigated by Gyorgyfalvy (1967) using the well-established e^N ($N \approx 9$) transition correlation rule of Smith & Gamberoni (1956). This is a purely empirical rule according to which disturbance introduced at an upstream location triggers transition to turbulence when its amplitude grows by a factor of e^N in accordance with the linear stability theory. Gyorgyfalvy's results indicated that spring-backed compliant membranes of suitable properties possess significant potential for delaying transition. It is pertinent to note that Gyorgyfalvy used the real phase speed c_r in place of the real group velocity to obtain the downstream spatial growth rates. Similarly favourable conclusions were tentatively reached by Carpenter & Garrad (1985) for certain of Kramer's walls, modelled as a bending plate backed by elastic foundation and viscous substrate, using a value of $N = 9.5$. Carpenter & Garrad also pointed out errors in the compliant membrane results of Landahl & Kaplan (1965).

By far the majority of drag reduction experiments to verify Kramer's discovery were conducted in turbulent flows. This preoccupation with turbulent-flow drag reduction could in part be a consequence of the relatively unfavourable assessment of the prospect for stabilization by the early works (such as those of Benjamin 1960, 1963 and Landahl 1962 already referred to), coupled with the particular circumstances of Kramer's experiment (conducted in Long Beach Harbor,

California). Experimental studies of drag reduction for laminar boundary layer and of the more fundamental aspects of stabilization connected with disturbance amplification are few. Aspects of such experimental works and even an account of the Russian works in the field, carried out by Babenko and co-workers, are described in Carpenter & Garrad (1985). Careful experiments to investigate the hydrodynamic stability of zero pressure-gradient flat-plate boundary-layer flow over compliant surfaces were recently initiated by Gaster at NMI Ltd. The experiments were performed in a large towing tank using speeds of up to 3 m/s. Preliminary findings, reported in Gaster (1984, 1985), indicated that the TSI waves do in fact suffer greatly reduced growth rate compared with similar waves in flow over a rigid plate; confirming the basic finding of Benjamin and others that wall compliance stabilizes the TS waves. A fuller account is now available in Gaster (1987).

In the present paper, we are concerned with the linear hydrodynamic stability of the Blasius boundary-layer flow over compliant walls which are composed of one or more uniformly thick layers of homogeneous, isotropic viscoelastic materials. These are normally backed by a rigid base as shown in figure 1. The bonding between the layers is assumed to be perfect so that there is no relative displacement between adjacent layers at their common interface. This is a more realistic model for compliant walls because such walls are more easily manufactured in practice than the idealized spring-backed membrane or plate surfaces investigated by many earlier studies.

The hydrodynamic stability of boundary-layer flow over non-dissipative layers was first studied qualitatively by Nonweiler (1963). Numerical solutions of the temporal stability eigenvalue problem were obtained by Kaplan (1964) and by Landahl & Kaplan (1965) for Voigt-type viscoelastic single layers subject to sliding type boundary condition at the interface between the layer and the rigid base. Some results for single- and two-layer walls were presented by Fraser & Carpenter (1985); these results appear to pertain only to elastic materials. Other recent works on flow stability of interest include those of Willis (1987) and Yeo (1986). Willis carried out stability calculations for some layered walls which corroborated very well with the amplification data obtained from Gaster's experiments. These results provide vindication for the use of the linear stability theory, a theory well tested for the rigid-wall case, in predicting the stabilization potential of compliant walls. The other major part of Willis (1987) concerns Carpenter-type Kramer surfaces. Compliant walls constituted of single or multiple layers of isotropic materials were studied in fairly extensive details by Yeo (1986). The influence of fibre-type material anisotropy on flow stability as well as the stability of the flow to three-dimensional wave modes was also investigated. The present paper reports on those parts of the work of Yeo (1986) which are devoted to the two-dimensional stability of boundary-layer flow over isotropic-material walls.

Section 2 below sets out the basic theory underlying the stability eigenvalue problem. The propagation of disturbance waves in the wall is described using a displacement-stress formalism which utilizes the wave-propagation solution of a single layer to represent the solution for any finite number of layers. Coupling between the flow and the wall perturbations is provided by the continuity of velocity and stress at the flow–wall interface. A preliminary version of the theory together with some viscoelastic single-layer and two-layer (the second layer being a solid layer or a viscous fluid substrate) wall results were presented by the author at the Euromech Colloquium 188 held at Leeds, UK in August 1984. Miscellaneous aspects of solutions, including a brief description of the major points of numerical

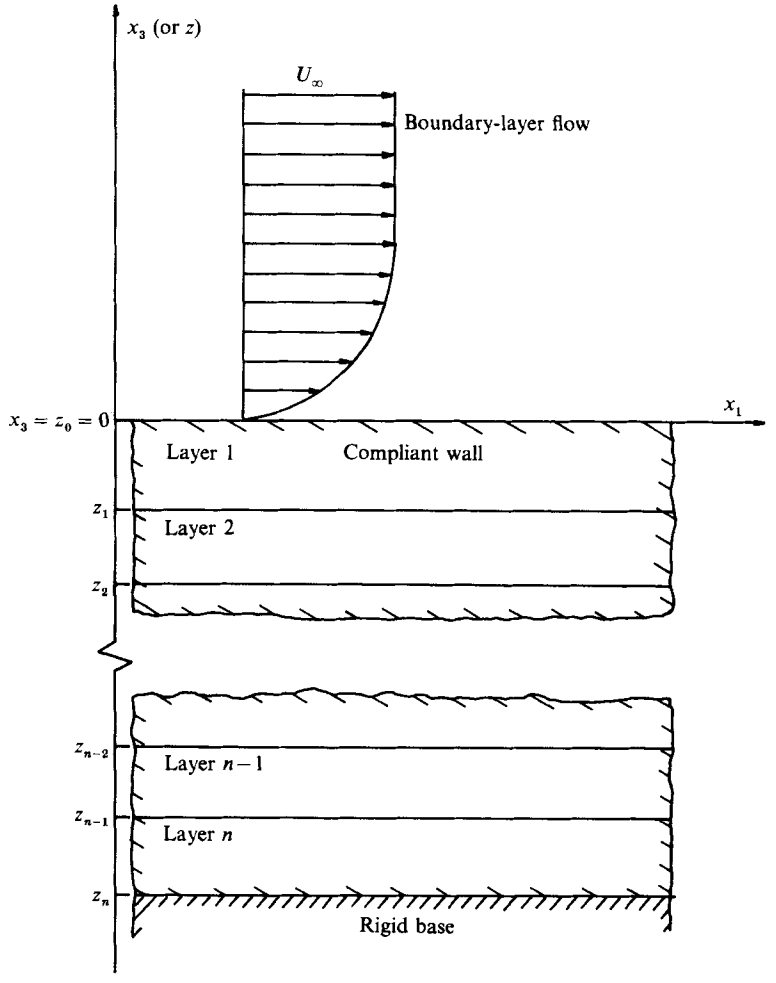

FIGURE 1. Boundary-layer flow over a multi-layer compliant wall.

implementation are covered in §2.6. In §3, results generated are compared against some of those available in the literature.

Results for single- and multi-layer walls are presented in §§4 and 5 respectively. The material densities are assumed to be equal to that of the flow, which may be assumed to be water. The need to investigate and understand the stability behaviour of multi-layer walls is very clear considering that the original Kramer walls, the genesis of the present subject, are in fact rather complicated multi-layer walls. Indeed, some of the compliant walls employed by Gaster in his recent experimental studies, already alluded to, are two-layer walls; consisting of a thin layer of a stiff material attached onto a much thicker and softer second layer. The addition of the stiff top-layer was found to have a beneficial effect on stability (Gaster, personal communication). In a less relevant case, Chung & Merrill (1984) reported that the attachment of a thin overlaying Teflon sheet onto soft viscoelastic layers suppressed surface deformation and produced some modest reduction in drag under turbulent flow conditions in a rotating disk apparatus. Multi-layer walls consisting of two to four compliant layers are investigated here. The four-layer walls studied bear a certain geometric similarity to the original Kramer walls. In addition to marginal

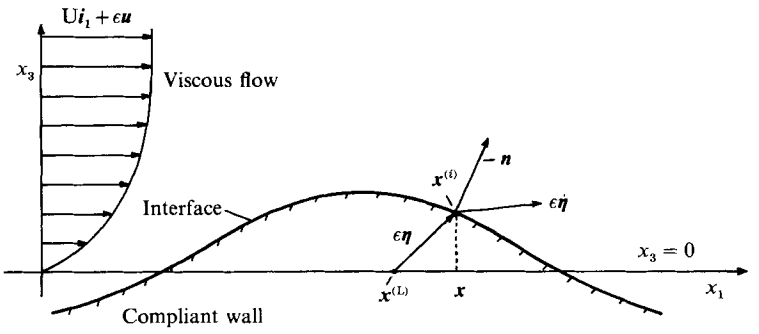

FIGURE 2. Flow-wall interface. $\boldsymbol{x} = (x_1, 0, 0)$; $\boldsymbol{x}^{(i)} = (x_1, 0, \epsilon\eta_3)$, coordinate of interface; $\boldsymbol{x}^{(L)} = (x_1^{(L)}, 0, 0)$, material coordinate of $\boldsymbol{x}^{(i)}$.

stability curves, the maximum spatial growth envelopes are also computed in a number of cases to assess the potential of selected walls for influencing transition. Wall eigenfunctions are also presented for a number of walls. These will be found to be invaluable in helping to explain various features of stability behaviour. Finally, in §6, flow eigenfunctions are discussed.

In this paper the consideration is restricted to two-dimensional disturbances propagating in the (x_1, x_3)-plane (see figure 2). While it is true that three-dimensional disturbance modes may be more dominant than two-dimensional ones in laminar boundary-layer flows over compliant walls as the study of Yeo (1986) shows, two-dimensional studies remain important and necessary on at least two counts. First, because of its much lower computational cost, the study of two-dimensional disturbance modes provides a useful preliminary assessment of the stability characteristics and this can be employed to identify suitable compliant walls that deserve more careful three-dimensional scrutiny. Furthermore, if the purpose is to eliminate or suppress the CIFI, then two-dimensional study will generally be adequate.

2. Theory

This section sets out the basic theory and notations. Important aspects of the numerical solution are very briefly outlined. Further details concerning both theory and numerical implementation are described in Yeo (1986).

2.1. *Flow stability equation*

The basic flow of interest here is the zero pressure-gradient boundary-layer flow over a flat surface. An important and often used approximation for this flow is given by the Blasius solution of Prandtl's boundary-layer equations. This is summarized below. In dimensionless form, the basic velocity profile is

$$U(x_3) = f'(x_3), \tag{2.1}$$

where $f(x_3)$ is the Blasius stream function which satisfies the ordinary differential equation

$$2f''' + m^2 f f'' = 0, \tag{2.2}$$

subject to the boundary conditions $f(0) = f'(0) = 0$ and $f'(\infty) = 1$. The prime denotes ordinary derivative with respect to x_3. The similarity reduction of Prandtl's

boundary-layer equations to the form given by (2.1) and (2.2) is obtained via the non-dimensionalization of velocities with respect to the free-stream velocity $U_\infty^{(d)}$ and lengths with respect to $\delta^{(d)}(= m(\nu^{(d)}x_1^{(d)}U_\infty^{(d)})^{\frac{1}{2}})$. Here $\nu^{(d)}$ is the kinematic viscosity and $x_1^{(d)}$, the distance from the leading edge. Superscript (d) is used to indicate that the quantity is dimensional. We take $\delta^{(d)}$ to be the local dimensional displacement thickness, in which case $m \approx 1.72078$.

In considering the linear stability of the Blasius boundary layer, it is further customary to disregard the non-parallel flow terms because these are asymptotically small at large values of the streamwise Reynolds number $R_x\,(=U_\infty^{(d)}x_1^{(d)}/\nu^{(d)})$. This renders the flow locally-parallel and considerably simplifies the stability analysis. If $\epsilon\boldsymbol{u} = (\epsilon u_1, 0, \epsilon u_3)^{\mathrm{T}}$ is a two-dimensional perturbation of the locally-parallel basic flow field $U(x_3)\boldsymbol{i}_1$ and $\epsilon\Phi$ the corresponding perturbation streamfunction (ϵ is a small real quantity) so that $u_1 = \Phi_{,3}$ and $u_3 = -\Phi_{,1}$, then in the normal mode analysis, Φ has a separable solution of the form $\phi(x_3)\,\mathrm{e}^{\mathrm{i}\alpha x_1}\mathrm{e}^{-\mathrm{i}\omega t}$ where $\phi(x_3)$ satisfies the Orr–Sommerfeld equation

$$(U-c)(\phi''-\alpha^2\phi)-U''\phi = \frac{1}{\mathrm{i}\alpha R_\delta}(\phi^{\mathrm{iv}}-2\alpha^2\phi''+\alpha^4\phi). \tag{2.3}$$

Here we note that ω and α are respectively the non-dimensional radian frequency and the x_1-wavenumber of the perturbation; $c\,(=\omega/\alpha)$ is the phase velocity. $R_\delta\,(=U_\infty^{(d)}\delta^{(d)}/\nu^{(d)})$ is the Reynolds number based on the local displacement thickness lengthscale $\delta^{(d)}$. We also note that the reference scale for stress is $\rho_{\mathrm{f}}^{(d)}\,(U_\infty^{(d)})^2$ where $\rho_{\mathrm{f}}^{(d)}$ is the dimensional density of the flow.

2.2. *Wave propagation in isotropic wall layers*

The propagation of sinusoidal waves in a homogeneous isotropic viscoelastic body with zero body forces is governed by the following dimensionless viscoelastic analogue of Navier's equation

$$\rho\frac{\partial^2}{\partial t^2}\boldsymbol{\eta} = \tfrac{1}{2}Y_{\mathrm{s}}\nabla^2\boldsymbol{\eta}+\left(\frac{2Y_\nu+Y_{\mathrm{s}}}{6}\right)\nabla\nabla\cdot\boldsymbol{\eta}, \tag{2.4}$$

where $\boldsymbol{\eta} = (\eta_1, \eta_2, \eta_3)^{\mathrm{T}}$ is the displacement vector field (see Bland 1960). All the physical quantities in this section are assumed to be non-dimensionalized with respect to the following reference scales; $U_\infty^{(d)}$ for velocity, $\rho_{\mathrm{f}}^{(d)}$ for density and $L_{\mathrm{w}}^{(d)}$ for length. The purpose of using a wall lengthscale $L_{\mathrm{w}}^{(d)}$, which differs from that of the 'local' flow, will become clear later on. Y_{s} and Y_ν are respectively the deviatoric and dilatational complex moduli and are related to the more familiar moduli of bulk K and shear G (both complex equivalents) by

$$Y_\nu = 3K, \quad Y_{\mathrm{s}} = 2G = 2\,(\rho C_{\mathrm{t}}^2-\mathrm{i}\omega d). \tag{2.5a, b}$$

ρ is the non-dimensional density. In the studies made, the materials were assumed to be elastic-dilatational (K real) and Voigt-deviatoric; which explains the form of G in (2.5b) where C_{t} and d are respectively the elastic shear speed and the damping coefficient of the material.

The displacement vector field $\boldsymbol{\eta}$ may be expressed as the sum of a curl-free field and a divergence-free field via the Stokes–Helmholtz decomposition as

$$\boldsymbol{\eta} = \nabla\phi^{(l)}+\nabla\times\boldsymbol{\psi}^{(l)}, \tag{2.6}$$

where $\phi^{(l)}$ and $\boldsymbol{\psi}^{(l)} = (\psi_1^{(l)}, \psi_2^{(l)}, \psi_3^{(l)})^{\mathrm{T}}$ are the Lame's potentials. Then $\boldsymbol{\eta}$ is a solution of (2.4) if $\phi^{(l)}$ and $\boldsymbol{\psi}^{(l)}$ satisfy the following wave equations

$$\left[\frac{\partial^2}{\partial t^2} - c_{\mathrm{L}}^2 \nabla^2\right] \phi^{(l)} = 0, \tag{2.7a}$$

$$\left[\frac{\partial^2}{\partial t^2} - c_{\mathrm{T}}^2 \nabla^2\right] \boldsymbol{\psi}^{(l)} = 0, \tag{2.7b}$$

where $$c_{\mathrm{L}}^2 = \frac{Y_\nu + 2Y_{\mathrm{s}}}{3\rho}, \quad c_{\mathrm{T}}^2 = \frac{Y_{\mathrm{s}}}{2\rho}.$$

The displacement fields $\nabla\phi^{(l)}$ and $\nabla \times \boldsymbol{\psi}^{(l)}$ correspond respectively to the propagation of dilatational (irrotational) and shear (equivoluminal) waves. c_{L} and c_{T} are hence commonly called the bulk wave speed and the shear wave speed respectively.

From the constitutive relation $\sigma_{kl} = Y_{\mathrm{s}} \epsilon_{kl} + \frac{1}{3}(Y_\nu - Y_{\mathrm{s}}) \delta_{kl} \epsilon_{jj}$ for sinusoidal type processes in isotropic viscoelastic solids (where $\epsilon_{kl} = \frac{1}{2}(\eta_{k,l} + \eta_{l,k})$ are the linear strain components), the stress components can be expressed in terms of the potentials $\phi^{(l)}$ and $\boldsymbol{\psi}^{(l)}$ using (2.6) to give

$$\sigma_{kl} = \tfrac{1}{3}(Y_\nu - Y_{\mathrm{s}}) \delta_{kl} \nabla^2 \phi^{(l)} + Y_{\mathrm{s}} \phi^{(l)}_{,kl} + \tfrac{1}{2} Y_{\mathrm{s}} (e_{kmn} \psi^{(l)}_{n,ml} + e_{lmn} \psi^{(l)}_{n,mk}), \tag{2.8}$$

where δ_{kl} is the Kronecker delta and e_{kmn} the alternating symbol. The usual convention on repeated indices and subscript commas is assumed.

The governing equations for the wall perturbations can be solved in closed form for the case of a single uniform layer. Since we are concerned here only with two-dimensional wave propagation, we look for plane strain ($\eta_2 = 0$) harmonic travelling-wave solution of the form

$$\phi^{(l)} = \hat{\phi}^{(l)} \mathrm{e}^{\mathrm{i}\alpha x_1} \mathrm{e}^{-\mathrm{i}\omega t}, \quad \boldsymbol{\psi}^{(l)} = (0, \hat{\psi}_2^{(l)}, 0)^{\mathrm{T}} \mathrm{e}^{\mathrm{i}\alpha x_1} \mathrm{e}^{-\mathrm{i}\omega t}. \tag{2.9a, b}$$

The substitution of these into the wave equations (2.7) yields two ordinary differential equations

$$\hat{\phi}^{(l)}_{,33} - b_{\mathrm{L}}^2 \hat{\phi}^{(l)} = 0, \quad \hat{\psi}^{(l)}_{2,33} - b_{\mathrm{T}}^2 \hat{\psi}^{(l)}_2 = 0, \tag{2.10a, b}$$

where $$b_{\mathrm{L}} = \alpha\left(1 - \frac{c^2}{c_{\mathrm{L}}^2}\right)^{\frac{1}{2}}, \quad b_{\mathrm{T}} = \alpha\left(1 - \frac{c^2}{c_{\mathrm{T}}^2}\right)^{\frac{1}{2}}.$$

These in turn have general solutions of the form

$$\hat{\phi}^{(l)} = B_1 \mathrm{e}^{b_{\mathrm{L}} x_3} + B_2 \mathrm{e}^{-b_{\mathrm{L}} x_3}, \quad \hat{\psi}_2^{(l)} = B_3 \mathrm{e}^{b_{\mathrm{T}} x_3} + B_4 \mathrm{e}^{-b_{\mathrm{T}} x_3}. \tag{2.11a, b}$$

The B_i ($i = 1, \ldots, 4$) are complex constants in a homogeneous layer and are determined when the boundary conditions of the layer are specified. With the solutions (2.11) for $\hat{\phi}^{(l)}$ and $\hat{\psi}_2^{(l)}$, we can determine the x_3-dependent complex amplitudes $\hat{\eta}_1$, $\hat{\eta}_3$, $\hat{\sigma}_{31}$ and $\hat{\sigma}_{33}$ in terms of the four constants B_1 to B_4 using (2.6) and (2.8), and form the vector $\boldsymbol{S}(x_3) = (\hat{\eta}_1, \hat{\eta}_3, \hat{\sigma}_{31}, \hat{\sigma}_{33})^{\mathrm{T}}$ which is referred to herein as the displacement-stress (d.s.) vector.

$$\boldsymbol{S}(x_3) = Q(x_3) \boldsymbol{B}, \tag{2.12a}$$

where $\boldsymbol{B} = (B_1, B_2, B_3, B_4)^{\mathrm{T}}$ and

$$\boldsymbol{Q}(x_3) = \begin{bmatrix} \mathrm{i}\alpha\, \mathrm{e}^{b_{\mathrm{L}} x_3} & \mathrm{i}\alpha\, \mathrm{e}^{-b_{\mathrm{L}} x_3} & -b_{\mathrm{T}}\, \mathrm{e}^{b_{\mathrm{T}} x_3} & b_{\mathrm{T}}\, \mathrm{e}^{-b_{\mathrm{T}} x_3} \\ b_{\mathrm{L}}\, \mathrm{e}^{b_{\mathrm{L}} x_3} & -b_{\mathrm{L}}\, \mathrm{e}^{-b_{\mathrm{L}} x_3} & \mathrm{i}\alpha\, \mathrm{e}^{b_{\mathrm{T}} x_3} & \mathrm{i}\alpha\, \mathrm{e}^{-b_{\mathrm{T}} x_3} \\ H_3\, \mathrm{e}^{b_{\mathrm{L}} x_3} & -H_3\, \mathrm{e}^{-b_{\mathrm{L}} x_3} & -H_1\, \mathrm{e}^{b_{\mathrm{T}} x_3} & -H_1\, \mathrm{e}^{-b_{\mathrm{T}} x_3} \\ H_1\, \mathrm{e}^{b_{\mathrm{L}} x_3} & H_1\, \mathrm{e}^{-b_{\mathrm{L}} x_3} & H_2\, \mathrm{e}^{b_{\mathrm{T}} x_3} & -H_2\, \mathrm{e}^{-b_{\mathrm{T}} x_3} \end{bmatrix} \tag{2.12b}$$

$H_1 = \frac{1}{2} Y_{\mathrm{s}}(\alpha^2 + b_{\mathrm{T}}^2)$, $H_2 = \mathrm{i}\alpha b_{\mathrm{T}} Y_{\mathrm{s}}$, $H_3 = \mathrm{i}\alpha b_{\mathrm{L}} Y_{\mathrm{s}}$.

The matrix $\boldsymbol{Q}$ is generally non-singular for layers of finite thicknesses. The d.s. vectors at two points in a layer, say $x_3 = z_1$ and z_2, can be related to each other by merely eliminating the 4-vector $\boldsymbol{B}$ to give

$$\boldsymbol{S}(z_2) = P(z_2, z_1)\, \boldsymbol{S}(z_1), \tag{2.13}$$

where $\boldsymbol{P}(z_2, z_1) = \boldsymbol{Q}(z_2)\, \boldsymbol{Q}^{-1}(z_1)$.

The matrix $\boldsymbol{P}$, called the propagation matrix, has the following properties: for arbitrary values of x_3 in the layer, say z_1, z_2 and z_3

$$\boldsymbol{P}(z_2, z_1) = \boldsymbol{P}^{-1}(z_1, z_2), \tag{2.14a}$$

and

$$\boldsymbol{P}(z_3, z_1) = \boldsymbol{P}(z_3, z_2)\, \boldsymbol{P}(z_2, z_1). \tag{2.14b}$$

From (2.14*a*), $\boldsymbol{P}(z_1, z_1)$ is the identity matrix. When the matrix function $\boldsymbol{P}(z_2, z_1)$ is known and the d.s. vector at one point z_1 specified, the d.s. vector at any other point z_2 in the layer is completely determined. From (2.14*b*) it can be shown that the linear relation between the d.s. vector at any two points in a given layer is independent of the origin of x_3 and is, in fact, dependent only on the distance between the two points; $\boldsymbol{P}(z_2, z_1) = \boldsymbol{P}(0, z_1 - z_2)$. The usefulness of the propagation matrix lies in the treatment of multi-layer wall response.

In a multi-layer wall such as that shown in figure 1, a different propagation matrix can be defined for each layer, and thus for the jth layer, the displacement-stress vector at the top of the layer ($x_3 = z_{j-1}$) and at the bottom of the layer ($x_3 = z_j$) are related by

$$\boldsymbol{S}(z_j) = \boldsymbol{P}^{(j)}(z_j, z_{j-1})\, \boldsymbol{S}(z_{j-1}), \tag{2.15}$$

where $\boldsymbol{P}^{(j)}$ is the propagation matrix for the jth layer. Since adjacent layers are assumed to be perfectly bonded together, the d.s. vector is continuous across the interfaces and a continuous d.s. vector can be defined over the entire compliant wall. The d.s. vector at the flow–wall interface at $x_3 = z_0 = 0$ can be related to that at the bottom of the nth layer at $x_3 = z_n$ by multiplying the propagation matrices together in the proper sequence

$$\begin{aligned} \boldsymbol{S}(z_n) &= \boldsymbol{P}^{(n)}(z_n, z_{n-1})\, \boldsymbol{S}(z_{n-1}) \\ &= \left\{ \prod_{j=n}^{j=1} \boldsymbol{P}^{(j)}(0, h^{(j)}) \right\} \boldsymbol{S}(z_0), \end{aligned} \tag{2.16}$$

where $h^{(j)} = z_{j-1} - z_j$ is the thickness of the jth layer. The bracketed superscript in this case denotes the layer number. When the nth layer is the last compliant layer and $x_3 = z_n$ is thus the interface with the rigid base, we call

$$\boldsymbol{P}^{\mathrm{O}} = \prod_{j=n}^{j=1} \boldsymbol{P}^{(j)}(0, h^{(j)}) \tag{2.17}$$

the overall propagation matrix of the compliant wall. The propagation matrix approach outlined above thus enables what happens at the top of the compliant wall to be propagated to the bottom of the last layer via the solution of a single layer. Historically, a method similar to the above was introduced by Thomson (1950) for the transmission of elastic waves through stratified solid medium. The present usage of the term propagation matrix follows that of Gilbert & Backus (1966).

2.3. *The coupling of fluid and wall motions*

Having established the necessary dynamics governing the perturbations in the flow and in the wall, it remains to relate these at the flow–wall interface, which has a mean and 'undisturbed' position along $x_3 = z_0$. As part of the linearity assumption, the disturbance wave amplitude $\epsilon|\boldsymbol{\eta}|$ at the interface is assumed to be much smaller than the wavelength so that the wave slope is also very small. The wall lengthscale $L_w^{(d)}$ is also used throughout this section.

Figure 2 shows a schematic view of the interface with greatly exaggerated wave amplitude. $\boldsymbol{U}^{(T)} = \boldsymbol{U}\boldsymbol{i}_1 + \epsilon\boldsymbol{u}$ is the perturbed two-dimensional local velocity profile. The superscript (T) denotes the 'total' of the entity; the sum of the mean and the perturbation. The superscript (L) denotes a material coordinate of the Lagrangian reference frame used for the description of wall motion. The coupling of the flow and the wall motions is provided by a kinematic and a dynamical interface conditions. These are

(i) the continuity of velocity at the interface

$$\epsilon\dot{\boldsymbol{\eta}}|_{\boldsymbol{x}^{(L)}} = \boldsymbol{U}^{(T)}|_{\boldsymbol{x}^{(i)}} \tag{2.18}$$

($\boldsymbol{x}^{(L)}$ and $\boldsymbol{x}^{(i)}$ are defined in figure 2) and

(ii) the continuity of stress at the interface

$$\underset{\text{(wall)}}{\sigma_{jk}^{(T)}|_{\boldsymbol{x}^{(L)}}} n_k = \underset{\text{(flow)}}{\sigma_{jk}^{(T)}|_{\boldsymbol{x}^{(i)}}} n_k, \quad (j = 1 \text{ and } 3), \tag{2.19}$$

where $\boldsymbol{n} = (n_1, n_2, n_3)^T$ is the unit normal in the direction of the vector

$$\left[-\epsilon\frac{\partial\eta_3}{\partial x_1^{(L)}}, \quad 0, \quad 1+\epsilon\frac{\partial\eta_1}{\partial x_1^{(L)}}\right]^T.$$

The above coupling conditions hold at the interface whose detailed position is not generally known in advance. Taylor expansions, however, enable these conditions to be approximated at the mean position of the interface at $x_3 = z_0 = 0$ to the same order of truncation accuracy as is implicit in the linearization applied. Taylor expansion of (2.18) about $\boldsymbol{x} = (x_1, 0, z_0)$ yields

$$\epsilon\dot{\boldsymbol{\eta}}|_{\boldsymbol{x}} - \boldsymbol{U}^{(T)}|_{\boldsymbol{x}} - \epsilon\eta_3\left[\frac{\partial\boldsymbol{U}^{(T)}}{\partial x_3}\right]_{\boldsymbol{x}} = O(\epsilon^2). \tag{2.20}$$

Since $U(z_0) = 0$, the x_1 and x_3-components of this equation are respectively

$$\dot{\eta}_1 = u_1 + U'\eta_3 + O(\epsilon), \tag{2.21a}$$

$$\dot{\eta}_3 = u_3 + O(\epsilon), \tag{2.21b}$$

where all the terms are evaluated at $\boldsymbol{x}$. To leading order, in terms of x_3-dependent complex amplitudes, we have

$$-\mathrm{i}\omega\hat{\eta}_1 = \phi'_{z_0} + U'|_{z_0}\hat{\eta}_3, \quad c\hat{\eta}_3 = \phi_{z_0}. \tag{2.22a, b}$$

The subscript z_0 denotes evaluation at $x_3 = z_0$. Equation (2.19) may be recast as

$$(\sigma_{jk}^{(m)} + \epsilon\sigma_{jk})|_{x^{(L)}} n_k = (\sigma_{jk}^{(m)} + \epsilon\sigma_{jk})|_{x^{(i)}} n_k \quad (j = 1 \text{ and } 3), \tag{2.23}$$

where the $\sigma_{jk}^{(m)}$ are the mean or equilibrium stresses. Expansion about $\boldsymbol{x}$ then gives

$$\sigma_{jk}^{(m)}|_x n_k - \epsilon\eta_1 \underbrace{\left[\frac{\partial\sigma_{jk}^{(m)}}{\partial x_1^{(L)}}\right]_x}_{\text{(wall)}} n_k + \epsilon\sigma_{jk}|_x n_k + O(\epsilon^2)$$
$$= \sigma_{jk}^{(m)}|_x n_k - \epsilon\eta_3 \underbrace{\left[\frac{\partial\sigma_{jk}^{(m)}}{\partial x_3}\right]_x}_{\text{(flow)}} n_k + \epsilon\sigma_{jk}|_x n_k + O(\epsilon^2) \quad (j = 1 \text{ and } 3). \tag{2.24}$$

The first terms on the right- and left-hand sides of the equality cancel because they represent the initial equilibrium state. The second term on the left-hand may be taken to be zero because it represents the streamwise variation of the mean stresses. Its omission is fully consistent with the locally parallel flow assumption. To leading order, in terms of complex amplitudes, it can be shown that

$$\hat{\sigma}_{31}|_{z_0} = \frac{1}{R_w}\left(\phi''_{z_0} + \alpha^2\phi_{z_0} + \frac{1}{c}U''|_{z_0}\phi_{z_0}\right), \tag{2.25a}$$

and

$$\underset{\text{(wall)}}{\hat{\sigma}_{33}|_{z_0}} = \frac{-1}{i\alpha R_w}\phi'''_{z_0} - \underbrace{\left(c + \frac{3i\alpha}{R_w}\right)}_{\text{(flow)}}\phi'_{z_0} - U'|_{z_0}\phi_{z_0}. \tag{2.25b}$$

where $R_w = U_\infty^{(d)} L_w^{(d)}/\nu^{(d)}$ is the Reynolds number based on the wall reference lengthscale. The term $U''|_{z_0}$ is zero for the Blasius velocity profile but need not be zero for the more general Falkner–Skan profiles.

Using (2.22) and (2.25), the d.s. vector for the wall at $x_3 = z_0$ can be defined in terms of the complex amplitude of the disturbance stream function ϕ and its derivatives at $x_3 = z_0$.

$$\boldsymbol{S}(z_0) = \boldsymbol{Q}_c(z_0)\,\boldsymbol{\varphi}_{z_0}^{(w)}, \tag{2.26a}$$

where $\boldsymbol{\varphi}^{(w)} = (\phi, \phi', \phi'', \phi''')^{T(w)}$ and

$$\boldsymbol{Q}_c = \begin{bmatrix} iU'(c\omega)^{-1} & i\omega^{-1} & 0 & 0 \\ c^{-1} & 0 & 0 & 0 \\ R_w^{-1}(\alpha^2 + U''c^{-1}) & 0 & R_w^{-1} & 0 \\ -U' & -(c + 3i\alpha R_w^{-1}) & 0 & -(i\alpha R_w)^{-1} \end{bmatrix}. \tag{2.26b}$$

The superscript (w) is placed for the sole purpose of emphasizing that the $\boldsymbol{\varphi}$ above is in the wall reference lengthscale of $L_w^{(d)}$. We call $\boldsymbol{Q}_c$ the flow-wall coupling matrix.

The coupling of tangential shear stress perturbation, included in the interface condition (2.19), was omitted in previous studies by Landahl & Kaplan (1965), Fraser (1984) and Fraser & Carpenter (1985). Instead these authors set $\hat{\sigma}_{31}|_{z_0}$ to zero on the ground that it is much smaller than the normal stress component $\hat{\sigma}_{33}|_{z_0}$. This omission is justifiable at moderate to large Reynolds numbers. For long wavelength disturbances at low Reynolds numbers, $\hat{\sigma}_{31}|_{z_0}$ may be of similar order to $\hat{\sigma}_{33}|_{z_0}$. Indeed long wavelength low Reynolds number instability was discovered by Craik (1966) for air flow over liquid layers. The retention of tangential shear stress coupling would enable such instabilities to be detected should they exist. Non-parallel flow effects will become important at low Reynolds numbers. However, it appears unlikely that they will nullify such instabilities should one really exist in the context of locally-parallel flow.

2.4. *Non-dimensionalization scheme*

The reader will have noted that different reference lengthscales have been adopted for the flow disturbance equations and for the description of wall response and the flow–wall coupling conditions; the other reference scales being identical. The local displacement thickness $\delta^{(d)}$ is a characteristic length of the boundary layer and the advantage of using it for flow calculation is that the local basic velocity profile is then independent of the Reynolds number R_δ. However, if $\delta^{(d)}$ is used as the reference lengthscale throughout the entire calculation, then, because the dimensional thicknesses and the other dimensional wall parameters are constant and $\delta^{(d)}$ varies streamwise with R_δ, it becomes necessary to scale all the dimensional wall parameters to a new local lengthscale $\delta^{(d)}$ each time R_δ changes. Such scalings must be done carefully and error has been known to occur. Instead of performing such rescaling of wall parameters at each R_δ, the approach used here is to perform all the calculations pertaining to the wall, and indeed also the coupling conditions in a fixed wall lengthscale $L_w^{(d)}$, which needs only be defined implicitly by the wall Reynolds number R_w ($= U_\infty^{(d)} L_w^{(d)}/\nu^{(d)}$), already introduced in the previous section. The overall propagation matrix $\boldsymbol{P}^O$ and the coupling matrix $\boldsymbol{Q}_c$ have already been defined using the wall lengthscale $L_w^{(d)}$. To link these with the flow calculations which are carried out in the local lengthscale $\delta^{(d)}$, it is only necessary to relate the flow disturbance amplitude vector $\boldsymbol{\varphi}_{z_0}^{(w)}$ of (2.26*a*) to its counterpart $\boldsymbol{\varphi}_{z_0}$ in the flow lengthscale of $\delta^{(d)}$. To do this, the lengthscale ratio $r = R_\delta/R_w = \delta^{(d)}/L_w^{(d)}$ is defined. Then

$$\boldsymbol{\varphi}_{z_0}^{(w)} = \boldsymbol{M}_s \boldsymbol{\varphi}_{z_0}, \tag{2.27}$$

where $\boldsymbol{M}_s$ is the diagonal matrix $\mathrm{Diag}\{r, 1, r^{-1}, r^{-2}\}$. Using (2.16), (2.17), (2.26) and (2.27) the d.s. vector at the interface with the rigid base $\boldsymbol{S}(z_n)$ can be related to the flow disturbance amplitude $\boldsymbol{\varphi}_{z_0}$ as follows

$$\boldsymbol{S}^{(w)}(z_n) = \boldsymbol{P}^{O(w)} \boldsymbol{Q}_c^{(w)} \boldsymbol{M}_s \boldsymbol{\varphi}_{z_0}. \tag{2.28}$$

Since all the calculations relating to the response of the wall are performed in the wall reference scales, it is therefore appropriate to specify the wall's material properties and dimensions in terms of the wall's references, which to recap are $L_w^{(d)}$, $U_\infty^{(d)}$ and $\rho_f^{(d)}$. In contrast with the other mentioned studies, the present non-dimensionalization procedure substitutes successive scalings of wall parameters with respect to $\delta^{(d)}$ with the simple calculation of the scaling matrix $\boldsymbol{M}_s$. The procedure is both simple to implement and less prone to errors. With (2.28), the boundary conditions to the Orr–Sommerfeld equation may now be specified.

2.5. *Boundary conditions for the Orr–Sommerfeld equation*

The Orr–Sommerfeld equation is a fourth-order ordinary differential equation and requires four boundary conditions for the problem to be fully specified. Two boundary conditions at $x_3 = z_0$ can be obtained from the first two rows of (2.28) if there is a specification of the displacement at the interface between the last layer and the rigid base. Since $\hat{\eta}_1|_{z_n} = 0$ and $\hat{\eta}_3|_{z_n} = 0$ when the last compliant layer is perfectly bonded onto the rigid base (this is so in almost all the cases examined) we have

$$\boldsymbol{Q}_L \boldsymbol{\varphi}_{z_0} = \boldsymbol{0} \text{ (null vector)}, \tag{2.29}$$

where $\boldsymbol{Q}_L$ is the 2×4 matrix formed from the first two rows of the product matrix $\boldsymbol{P}^{O(w)} \boldsymbol{Q}_c^{(w)} \boldsymbol{M}_s$.

The other two boundary conditions are given by the requirement that the disturbance amplitude $\phi(x_3)$ must remain bounded as $x_3 \to \infty$. As $x_3 \to \infty$, $U(x_3)$ tends to unity and the Orr–Sommerfeld equation reduces to

$$(\mathrm{D}^2-\alpha^2)(\mathrm{D}^2-\beta^2)\phi = 0 \quad \left(\mathrm{D} \equiv \frac{\mathrm{d}}{\mathrm{d}x_3}\right), \tag{2.30}$$

where $\beta = (\alpha^2+\mathrm{i}\alpha R_\delta(1-c))^{\frac{1}{2}}$, $\beta_\mathrm{r} > 0$ and $\alpha_\mathrm{r} > 0$. Subscript r denotes the real part of the complex quantity. Admissible solutions of (2.30) which remain bounded at $x_3 = \infty$ have the form

$$\phi = B_1 \mathrm{e}^{-\alpha x_3} + B_2 \mathrm{e}^{-\beta x_3}, \tag{2.31}$$

where B_1 and B_2 are complex constants. Assuming a sufficiently high degree of differentiability for $\phi(x_3)$, it can be shown using (2.31) that the following relation holds for ϕ at large values of x_3:

$$\boldsymbol{Q}_\infty \boldsymbol{\varphi} = \mathbf{0}, \tag{2.32}$$

where

$$\boldsymbol{Q}_\infty = \begin{bmatrix} \alpha\beta & \alpha+\beta & 1 & 0 \\ 0 & \alpha\beta & \alpha+\beta & 0 \end{bmatrix}.$$

The Orr–Sommerfeld equation and the four homogeneous boundary conditions given by (2.29) and (2.32) then constitute the necessary eigenvalue problem. This eigenvalue relation may be denoted symbolically as

$$\mathscr{F}(\alpha, \omega, R_\delta) = 0, \tag{2.33}$$

where the dependence on wall parameters is suppressed for notational brevity. When considering stability in the spatial sense, a disturbance wave of fixed real frequency ω is said to be unstable when $\alpha_\mathrm{i} < 0$ (subscript i denotes the imaginary part of the quantity). This corresponds physically to a downstream growing wave. The neutral states (both ω and α are real) for both temporal and spatial considerations are, however, identical.

At this juncture, it is appropriate to mention an extension to the theory of §2.2 for the case in which there is no rigid base, but instead, the nth or last layer is an infinite half-space extending to $-\infty$ in the x_3-direction. This half-space idealization is also useful for treating cases in which the rate of disturbance decay within certain layers is so rapid that it is not possible within the available floating-point accuracy to 'propagate' the disturbance across the layer. This happens, for example, when the thickness of the layer is fairly large compared with the propagating wavelength of the disturbance. If the nth layer is the half-space, solutions are admissible only when the d.s. vector $\boldsymbol{S}(x_3)$ remains bounded as x_3 tends to $-\infty$. From the theory in §2.2, we note that the constant 4-vector of the nth layer $\boldsymbol{B}^{(n)} = \boldsymbol{P}^{\mathrm{O}}\boldsymbol{S}(z_0)$ where $\boldsymbol{P}^{\mathrm{O}}$ is now redefined to be

$$\boldsymbol{P}^{\mathrm{O}} = \boldsymbol{Q}^{-1}(z_{n-1}) \prod_{j=n-1}^{1} \boldsymbol{P}^{(j)}(0, h^{(j)}). \tag{2.34}$$

The requirement that the disturbance amplitude remains bounded as $x_3 \to -\infty$ implies that those components of $\boldsymbol{B}^{(n)}$ which correspond to growing waves as $x_3 \to -\infty$ must be set to zero. When $(b_\mathrm{L})_\mathrm{r}$ and $(b_\mathrm{T})_\mathrm{r}$ are greater than zero, the components are $B_2^{(n)}$ and $B_4^{(n)}$. The boundary condition matrix $\boldsymbol{Q}_\mathrm{L}$ in (2.29) must now be formed from the second and fourth rows of $\boldsymbol{P}^{\mathrm{O}(\mathrm{w})}\boldsymbol{Q}_\mathrm{c}^{(\mathrm{w})}\boldsymbol{M}_\mathrm{s}$ where $\boldsymbol{P}^{\mathrm{O}}$ is now given by (2.34).

2.6. *Numerical and other aspects of solution*

An initial-value or 'shooting' approach was adopted to solve the eigenvalue problem represented symbolically by (2.33). The particular variant used to compute $\mathscr{F}$ employs the compound matrix formulation of Ng & Reid (1979) for the Orr–Sommerfeld equation. The compound-matrix equivalent of the Orr–Sommerfeld equation does not suffer from the parasitic growth problem associated with the highly 'stiff' nature of the equation at large R_δ. Its integration can hence be performed using any standard integration routine for ordinary differential equations. In the present investigation, the integration of the compound-matrix equivalent was carried out using the Adam's routine DO2QAF of the NAG Routine Library. This is a more sophisticated routine than the commonly used fixed step-size fourth-order Runge–Kutta routine. It employs a variable step-size and variable order strategy to calculate its results to within a specified bounding tolerance for local errors. A local error tolerance of 10^{-8} with a mixed-error criterion was found to be completely adequate (see Routine's documentation). Because of the variable step-size nature of the integration routine, the basic flow equation (2.2) was simultaneously integrated with the governing equation. This incurred additional, though generally small, computational cost. A better alternative, which avoids the numerous re-integration of the basic flow equation, would be to provide the required basic flow data by employing Chebyshev polynomial representations for the Blasius solution and its derivatives. This latter course was adopted for some of the three-dimensional stability studies reported in Yeo (1986).

The infinity boundary conditions given by (2.32) were implemented at $x_3 = 6$ (displacement thicknesses). This is more than twice the boundary-layer thickness based on $0.99U_\infty$. The results obtained were practically identical to those obtained with $x_3 = 8$. The eigenvalues or the roots of the relation (2.33) are determined in an iterative manner using the root finder C05NBF of the NAG routine library. This is a general nonlinear equation solver which is based on a modified version of the Powell's hybrid method. The level of convergence was fixed at 10^{-7} for almost all the runs. This gives, when the initial guess values are scaled to unity, a uniform accuracy of 7 significant decimal digits in all the components of the roots (see Routine's documentation). Further details of numerical implementation can be found in Yeo (1986) which also describes a global search scheme for unstable eigenstates.

When an eigenvalue of the problem has been found, the corresponding disturbance eigenfunction of the flow may be calculated (see Davey 1981 or Yeo 1986). The displacement-stress vector at a point $x_3 = z$ in the ith layer is then given recursively by

$$\boldsymbol{S}(z) = \boldsymbol{P}^{(i)}(0, z_{i-1} - z)\, \boldsymbol{S}(z_{i-1}), \tag{2.35a}$$

and

$$\boldsymbol{S}(z_0) = \boldsymbol{Q}_{\mathrm{c}}^{(\mathrm{w})} \boldsymbol{M}_{\mathrm{s}} \boldsymbol{\varphi}_{z_0}. \tag{2.35b}$$

From (2.35) the distributions of the complex strain amplitudes $\hat{\epsilon}_{ij}$ can be computed from the distributions of $\hat{\eta}_1$ and $\hat{\eta}_3$. For a neutral eigenstate, the average local rate of dissipation per unit volume within the compliant wall is

$$\dot{D} = \overline{(\sigma_{ij})_{\mathrm{r}}\, (\epsilon_{ij})_{\mathrm{r}}} = d(\omega^{(\mathrm{w})})^2 \sum_{ij} |\hat{e}_{ij}|^2, \tag{2.36}$$

where $\hat{e}_{ij} = \hat{\epsilon}_{ij} - \frac{1}{3}\delta_{ij}\hat{\epsilon}_{kk}$ are just the complex amplitudes of the deviatoric strain components. The overbar denotes averaging over the phase of the wave. The second equality in (2.36) holds for the special case of elastic-dilatational and Voigt-

deviatoric materials (see equation (2.5*a*, *b*)) studied here. For a Voigt material, a measure of the 'quality' of the damping is given by the loss tangent

$$\tan\delta = (\omega^{(w)}d)/(\rho C_t^2), \tag{2.37}$$

where δ is the phase angle, called the loss angle, by which the strain lags the stress.

The linear theory contains an arbitrary scaling factor. To compare the response of different compliant walls, the wall eigenfunctions are normalized so that $\hat{\eta}_3|_{z_0} = 1$. This normalization is, however, not particularly useful for the flow eigenfunctions because $\hat{\eta}_3|_{z_0}$ must be zero for a rigid wall. To allow comparisons with rigid-wall cases, flow eigenfunctions are normalized in such a way that the mean kinetic energy density of the disturbance, defined as $\overline{(u_i)_r (u_i)_r}$, is unity at $x_3 = 6$ (the outer integration limit). Furthermore, the phase of $(\mathrm{d}/\mathrm{d}x_3)\hat{u}_1$ at $x_3 = z_0$, the flow-wall interface, is fixed at $-\frac{1}{4}\pi$.

The total or integrated spatial growth of disturbances having fixed values of the non-dimensional frequency $F = \omega/R_\delta$ is investigated to assess the potential of certain compliant walls to influence transition. The exponential growth factors between two streamwise locations denoted s_0 and s are calculated according to

$$\ln\left[\frac{|A_s|}{|A_0|}\right] = -\frac{2}{m^2}\int_{R_\delta(s_0)}^{R_\delta(s)} \alpha_i \,\mathrm{d}R_\delta, \tag{2.38}$$

where $|A|$ is a suitably defined disturbance amplitude of the flow.† s_0 is usually chosen to correspond to points on the lower branch of the neutral curve.

3. Comparison with some published results

3.1. *Blasius flow over a rigid flat plate*

Before a systematic study of viscoelastic wall layers was begun, a detailed study was made of the stability of Blasius flow over a rigid flat plate. The marginal stability curve and the spatial amplification rate contours ($\alpha_i = -0.005$ and $\alpha_i = -0.01$) were computed and these are compared against the published results of Jordinson (1970) in figure 3. The agreement with the marginal stability data of Jordinson's table 1 is generally to 3 or 4 significant digits. The agreement with Jordinson's spatial amplification data does not seem to be as good, mainly because the data had to be scaled from his figure 3. Calculations of total spatial amplification (at fixed values of the non-dimensional frequency $F = \omega/R_\delta$) as well as disturbance eigenfunctions and Reynolds stresses also show very good agreement with those of Jordinson. Furthermore, at the streamwise Reynolds numbers R_x of 2.84×10^6 ($R_\delta \approx 2900$) and 4.9×10^6 ($R_\delta \approx 3809$), which are the experimentally observed transition Reynolds numbers of Schubauer & Skramstad (1948) and Wells (1967) respectively, the maximum amplification factors are approximately $e^{8.28}$ and $e^{11.83}$ respectively. These values are almost identical to those quoted by Jaffe, Okamura & Smith (1970), which are $e^{8.3}$ and $e^{11.8}$ respectively at the two transition locations. Jaffe *et al.* employed a

† Non-parallel flow contributions to the local spatial growth rate $|A|^{-1}(\mathrm{d}|A|/\mathrm{d}x_1)$ may, to a first approximation, be estimated from the flow eigenfunctions (see Gaster 1974). These were neglected above because they are asymptotically small at large R_x; being of the order of $1/(R_x)^{\frac{1}{2}}$ when compared with the parallel-flow growth rate of α_i. Their contributions to the integrated or total spatial growth may, however, be of some significance; a point suggested by Professor M. Gaster to the author. It is hoped that this can be looked into in the near future.

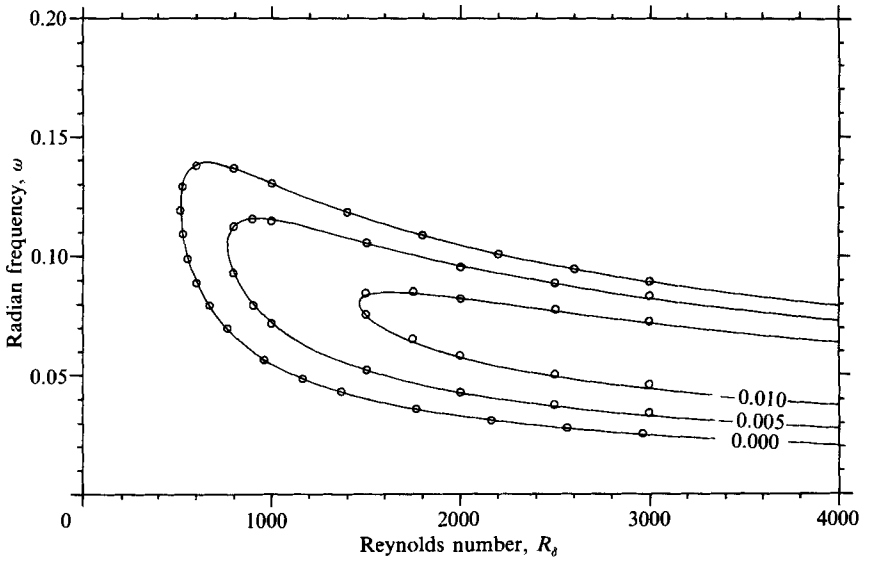

FIGURE 3. Curves of constant α_i for Blasius boundary-layer flow over a rigid wall. ——, present results; ○, Jordinson (1970).

Gram–Schmidt orthogonalization technique to overcome the numerical difficulties associated with the stiff nature of the Orr–Sommerfeld equation.

As a particularly severe test of the numerical method adopted and the codes, a single eigenvalue calculation was performed at a large Reynolds number $R_\delta = 1.72078 \times 10^6$ and $\alpha = 0.30802099$. The temporal eigenvalue c obtained has the value $0.321663 - 0.036287i$, in almost complete agreement with the value of $0.32166 - 0.03629i$ quoted in Davey (1981). The eigenfunctions at this eigenstate were also calculated and they display excellent agreement with figure 1 of Davey, which shows the wave-packet nature of the disturbance. Davey also mentioned a critical Reynolds number of $R_\delta = 519.06$ at $\alpha = 0.30377$. The value of $R_\delta = 519.062$ was obtained by the present author at the same value of α.

3.2. *The rubber-layer walls of Kaplan and Landahl*

Stability calculations were also performed on two of Kaplan's incompressible rubber-layer walls of uniform thickness and the results are compared in figure 4. Kaplan's compliant layers were not firmly bonded onto the rigid base, but were allowed to slide freely at the interface subject to zero vertical displacement instead. The boundary conditions at the interface with the rigid base are thus those of zero vertical displacement and zero shear stress perturbation, and were intended to simulate the dolphin's coating which was supposed to be loosely anchored onto a firmer muscular base. These boundary conditions present no difficulty to the theoretical formulation developed in §2. In this case, the matrix $\boldsymbol{Q}_L$ in (2.29) is formed from the second and third rows of the product matrix in (2.28). The displayed data points in figure 4 were scaled from figure 10 of Landahl & Kaplan (1965). There is reasonably good agreement except near the noses of the unstable domains where the present results show slightly lower critical Reynolds numbers R_δ^{cr}. These discrepancies are not unexpected for on top of the various detailed computational differences, Kaplan's model had omitted to couple the tangential shear stress perturbation at the flow–wall interface. Perturbation shear stress coupling is

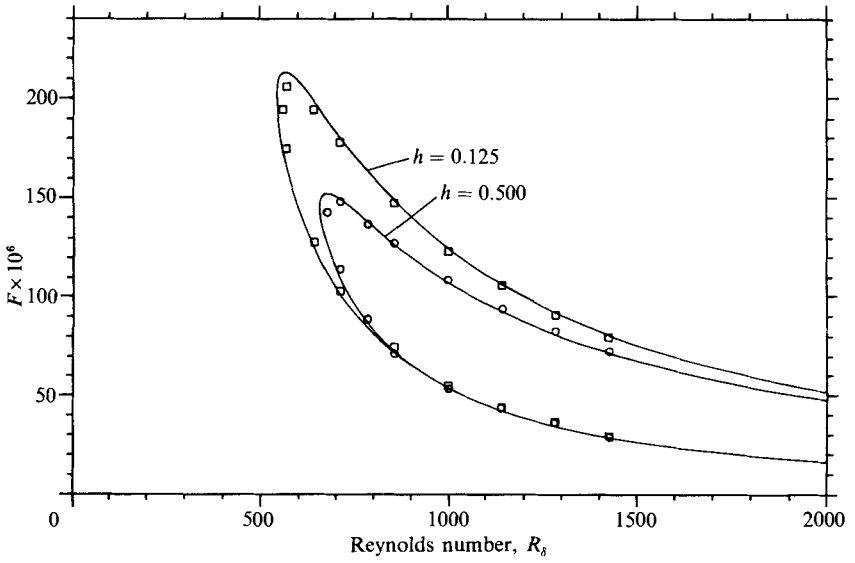

FIGURE 4. Marginal stability curves of free-sliding incompressible viscoelastic layers with $\rho = 1.2$, $C_t = 0.8$ and $d = 0.0125$. ——, present results; □, ○, Landahl & Kaplan (1965).

incorporated in the present theoretical scheme. Indeed, according to Landahl & Kaplan, asymptotic analysis showed that the inclusion of shear stress coupling should have a mildly destabilizing effect, and this seems to be consistent with the differences noted. While its omission is fully justified at large Reynolds numbers, shear stress perturbation could be important at low Reynolds numbers.

4. Single-layer viscoelastic walls

This section is devoted to the consideration of Blasius boundary-layer flow over single-layer viscoelastic walls. The bonding between the layer and the rigid base is assumed to be perfect so that $\hat{\eta}_1|_{z_1}$ and $\hat{\eta}_3|_{z_1}$, the displacement amplitudes at the interface with the rigid base, are both zero. This is more realistic for a practical device than the sliding interface condition used by Landahl & Kaplan (1965). The single-layer study also furnishes a useful starting point for multi-layer cases where many more parameters of the wall must be specified. To accord with the non-dimensionalization scheme described in §2.4, all the wall parameters (dimensions and properties) are given in terms of the wall's set of reference scales. The wall Reynolds number R_w is set at 2×10^4 in all cases. Unless otherwise indicated, the non-dimensional densities of the materials that made up the compliant walls are all assumed to be 1.0.

4.1. *The instabilities and their dominant nature*

Figure 5 displays the spatial stability characteristics for a single-layer wall which has a layer thickness of $h = 1.0$, $C_t = 0.7$ and a relatively low material damping coefficient of $d = 0.0049$ (note that these are specified in wall reference scales). The material is nearly incompressible because of the relatively high value of the Bulk modulus ($K = 500$).

Three distinct regions of instability can immediately be discerned. The unstable states in regime A are the direct derivatives of the Tollmien–Schlichting instability

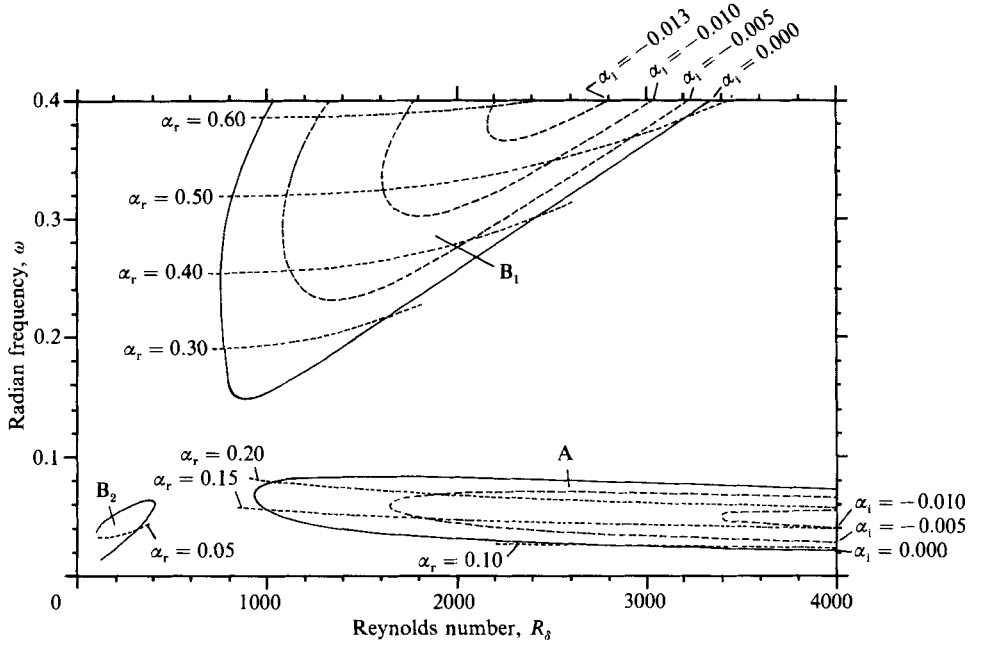

FIGURE 5. The stability diagram for a layer with $h = 1.0$, $C_t = 0.7$, $d = 0.0049$ and $K = 500$.

(TSI) that arises in similar flow over a rigid wall. These instabilities are Class A in Benjamin's classification. The instabilities in regimes B_1 and B_2 have arisen as a consequence of the compliant quality of the wall and are hence a type of CIFI. As will be seen, these latter modes are resisted by wall damping and are hence Class B in Benjamin's scheme. The alphabet in the names of the regimes have been specifically chosen to reflect the 'energy' character of the instability under Benjamin's classification. The numeral subscripts are introduced to distinguish the different instability regimes in the same 'energy' class; thus allowing for more precise referencing of the instabilities.

The stabilizing influence of wall compliance on the TSI is well known and may be seen by comparing figures 3 (rigid-wall case) and 5. In addition to having a significantly higher critical Reynolds number R_δ^{cr} ($\simeq 935$), at any given R_δ, the unstable A regime has reduced maximum spatial growth rates (α_i) and a narrower band of unstable frequencies (ω). This gain in stability is, however, largely negated by the existence of the compliance-induced unstable regimes B_1 and B_2. The unstable regime B_1 is by far the most extensive. It has a lower R_δ^{cr} ($\simeq 758$) than the A regime and its maximum local spatial growth rates are more than twice those of the unstable A regime at the same R_δ, over the range of R_δ shown. Figure 6 gives the maximum amplification envelope for the unstable A regime and the total amplification curves at two values of F for the unstable B_1 modes. Thus for this wall, wall compliance potentially leads to early transition via the CIFI modes.

The unstable B_2 regime stretches to small R_δ and a critical Reynolds number R_δ^{cr} in the usual sense cannot be ascribed. In the low R_δ range, the locally-parallel flow assumption cannot be regarded as valid. The existence of the B_2 regime, more generally, however, does not appear to be in doubt even if non-parallel effects are considered because, for certain compliant walls, this regime can stretch to R_δ as large as 2000. The spatial growth rates are, however, very low and from the viewpoint of

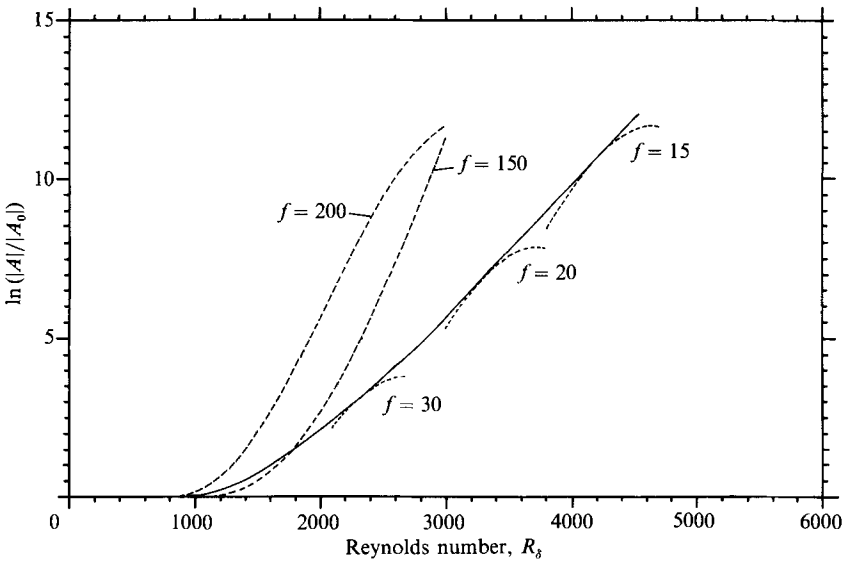

FIGURE 6. The maximum amplification envelopes for the compliant wall of figure 5. ——, maximum amplification envelope; - - - - -, total amplification curves at $F = f \times 10^{-6}$ (Class A), – – – – –, total amplification curves at $F = f \times 10^{-6}$ (Class B_1).

integrated downstream growth, the B_2 regime does not appear to pose a serious threat to the longer-term (downstream) stability of the flow.

Other than the differences in their response to wall damping, which have been used to categorize the instabilities into Class A and Class B, the three unstable regimes possess other distinctive features that are worth noting. In general, the neutral and unstable B_1 and B_2 eigenstates have higher real phase velocity c_r than similar A eigenstates. While c_r is almost always less than 0.5 for neutral and unstable Class A TSI waves, it can assume values close to 1.0 for unstable B_1 and B_2 waves. From figure 5 it is seen that the unstable B_1 modes tend to possess larger values of real wavenumber α_r than the unstable A modes at corresponding R_δ. The unstable B_2 waves have low α_r and are hence a form of long-wave disturbance. This indicates that the instability may be related to the long-wave instability found in air flow over liquid layers (Craik 1966); which has its origin in the fluctuating interface shear stresses. Study of the B_2 neutral eigenstates, in particular those on the lower branch of the B_2 loop, shows that at the lower R_δ end of the loop, the perturbation shear stress $\hat{\sigma}_{31}$ at the flow–wall interface may be of the same order of magnitude as the vertical stress $\hat{\sigma}_{33}$. While non-parallel flow influence is certain to become important at low R_δ, its effect is probably one of mild destabilization similar to the effect it has on rigid-wall TSI modes. The distribution of α_r contours in figure 5 indicates that the real group velocity $(\delta\omega/\delta\alpha)_r$ is positive at all the unstable eigenstates.

The compliant wall that has just been discussed cannot be said to be a typical single-layer wall because both significant and complex changes in the stability characteristics take place when the wall parameters are altered. It is, nevertheless, a useful reference case and a starting point for further detailed investigation into the effects the various wall parameters have on the stability of the coupled system.

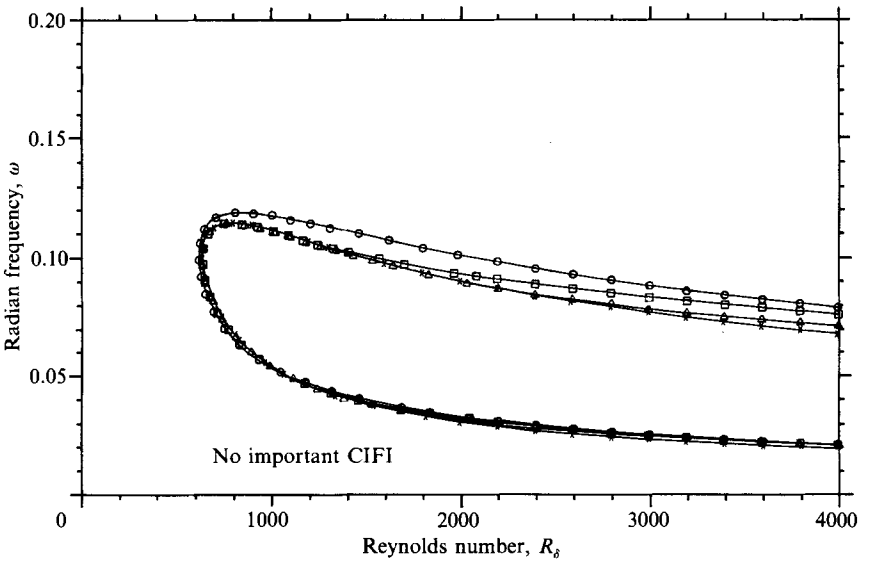

FIGURE 7. Effects of layer thickness h on the marginal stability curves for a layer with $C_t = 1.0$, $d = 0.0049$ and $K = 500$. ○, $h = 0.4$; □, $h = 1.0$; △, $h = 2.0$; ×, $h = 5.0$.

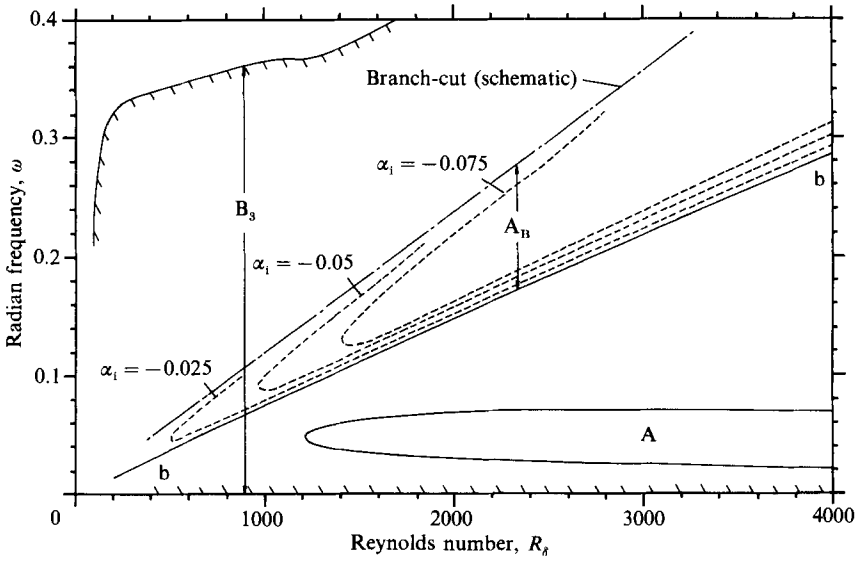

FIGURE 8. The marginal stability curves for a single-layer wall with $h = 1.0$, $C_t = 0.5$, $d = 0.0049$ and $K = 500$.

4.2. *The effects of material stiffness and thickness of the layer on stability (single-layer)*

The material stiffness of the wall is determined by C_t, where C_t is the shear velocity the material would have if there were no damping (see §2.2). The effects of changing the C_t on the stability characteristics of the wall discussed in the immediately preceding section can be seen from figures 7 and 8. It is observed that an increase in C_t strongly inhibits the B_1 and B_2 instabilities, whose existence is a consequence of wall compliance. For $C_t = 1.0$ ($h = 1.0$) shown in figure 7, there are no significant

unstable B_1 and B_2 modes. There is a very small remnant of the unstable B_2 regime which continues to persist at very low Reynolds numbers, typically less than 100. These modes are not illustrated in figure 7 because in this range of R_δ, there are strong non-parallel flow effects and the true existence of these modes is questionable. At $C_t = 1.0$ ($h = 1.0$), the critical Reynolds number R_δ^{cr} is reduced to about 642 and there is a significant increase in the ω-bandwidth of the unstable A regime over that for $C_t = 0.7$. Increase in the unstable ω-bandwidth generally indicates an increase in the local amplification rates. Increase in C_t, other things being equal, is therefore stabilizing for the B_1 and B_2 CIFI modes but destabilizing for the A or the TSI modes. Reduction in the C_t has just the opposite effect on the stability. Figure 8 shows the marginal stability curves for a wall with $C_t = 0.5$, $h = 1.0$ and $d = 0.0049$. The R_δ^{cr} for the unstable A regime is now increased to approximately 1208, which is more than twice the rigid-wall value. There is also a large contraction of the unstable A regime. This is, however, accompanied by a very significant change in the topology as well as a very strong intensification of the unstable Class B CIFI modes. As C_t is reduced from 0.7 to 0.5, it appears that the B_1 and B_2 regimes coalesce and then develop into two large regimes of instability, one overlaying the other.

The larger of the two unstable regimes, which is hashed on the unstable side of the marginal curves, stretches to frequency ω less than 0.001, and possibly even lower to zero frequency. The existence of similar zero/near-zero frequency modes may also be seen in figure 14 of Carpenter & Garrad (1985) for boundary-layer flow over compliant walls which are modelled as a plate on an elastic foundation and in figures 6 and 7 of Gyorgyfalvy (1967) for similar flow over spring-backed membranes with viscous damping. Gyorgyfalvy referred to them as divergence-type Class C instability and in both of his figures these instabilities set in when the stiffness of the wall (the membrane's free wave speed and the foundation stiffness parameter) is sufficiently low. As we shall see further on, these unstable modes seem to be of Class B character and are hence referred to here as B_3 modes. A possible connection between the occurrence of the near-zero frequency instability and the violation of the static criterion for inviscid flow over passive compliant walls (Yeo & Dowling 1987) was suggested by Yeo (1986).

The smaller regime is bounded above by what appears to be branch-cut behaviour in the α-plane. As ω is increased at a given R_δ from the lower marginal curve b–b, a stage is soon reached at which α_r begins to tend to zero. When this happens, the real phase velocity c_r rises rapidly to values much larger than 1.0. These unstable modes appear to have a Class A character with respect to increase in damping, and shall be referred to herein as A_B modes to distinguish them from the unstable Class A modes of Tollmien–Schlichting origin.

The maximum local spatial growth rates α_i in the unstable B_3 and A_B regimes of figure 8 are found to be very much larger than those of the A regime at the same R_δ; as much as 10 times as high and they thus represent very strong instabilities. Some constant α_i contours for the unstable A_B regime are shown. We shall have more to say concerning these highly unstable modes later on. It suffices to note that at low C_t, such as 0.5, there are potentially strong instability regimes that stretch to very low frequencies and low Reynolds numbers R_δ.

Increasing the wall thickness evidently destabilizes all the CIFI regimes. At $C_t = 0.7$, there are no longer separate B_1 and B_2 regimes for the thickness $h = 5.0$. Figure 10(*a*) illustrates what has occurred. When $h = 0.4$ (thin layer) no significant Class B instabilities occur in the R_δ, ω range shown. An increase in the thickness h to 1.0 results in a very rapid onset of Class B instabilities. A further increase causes the

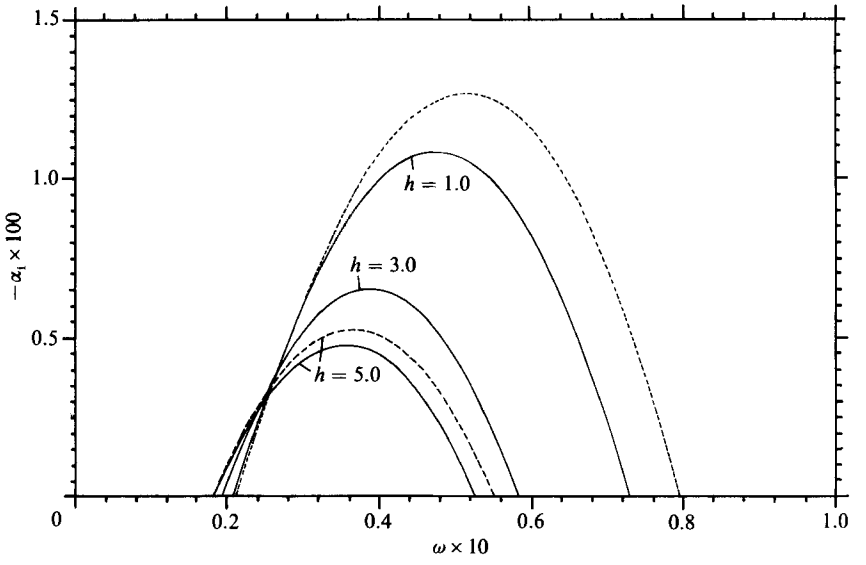

FIGURE 9. Spatial amplification rates at Reynolds number of 4000 for a layer with $C_t = 0.7$ and $K = 500$. ——, $d = 0.0049$; – – – –, $d = 0.0588$; ------, rigid wall.

unstable B_1 and B_2 regimes to coalesce or merge into a single large unstable Class B regime and a shift of the lower neutral boundary to lower ω. For $h = 5.0$, calculations indicate that the group velocities of the unstable Class B spatial eigenstates along $R_\delta = 2000$ and $R_\delta = 4000$ have positive real parts and relatively small imaginary parts. The real group velocities are less than 1.0.

From the results presented so far, it may be seen that an increase in wall compliance, which may either be derived from a reduction in C_t or an increase in the wall thickness h, leads to instabilities shifting to lower frequencies. It is interesting to note that the lower neutral boundaries of the merged B_1 and B_2 regimes and the A_B regime are almost straight lines joining the origin in the (R_δ, ω)-plane suggesting that these instabilities only set in above certain dimensional frequencies; depending weakly only on the Reynolds numbers R_δ. The global aspect of these instabilities is in marked contrast with that of the unstable A or TSI regime which at any dimensional frequency has a fairly limited range of unstable R_δ.

The effects of the layer thickness h on the unstable A regime of a layer with $C_t = 0.7$ and $d = 0.0049$ are depicted in figure 10(*b*). It is observed that the wall thickness h only has a limited influence on the critical Reynolds number R_δ^{cr}, being significant only when the layer is relatively thin. Beyond $h = 2.0$, the effect of h on the R_δ^{cr} is minute. The maximum R_δ^{cr} that can be obtained for this material by increasing h is only about 1036, about twice the rigid-wall value. The effect of h on the ω-bandwidth of the A regimes is, however, more significant. There is still a very evident reduction in the ω-bandwidth of the regime at $R_\delta = 4000$ for h varying between 3.0 and 5.0 although the critical Reynolds number R_δ^{cr} is practically identical. The local amplification rates of the unstable Class A waves at $R_\delta = 4000$ for the various wall thicknesses $h = 1.0$, 3.0 and 5.0, and for the rigid wall are given in figure 9. It can be seen that a very significant reduction in the growth rates accompanies the reduction in the ω-bandwidth of the A regimes. At $h = 5.0$, the maximum local spatial growth rate is less than 40% that of the rigid-wall maximum. It can hence be seen that while the increase in h may have the beneficial effect of reducing the local

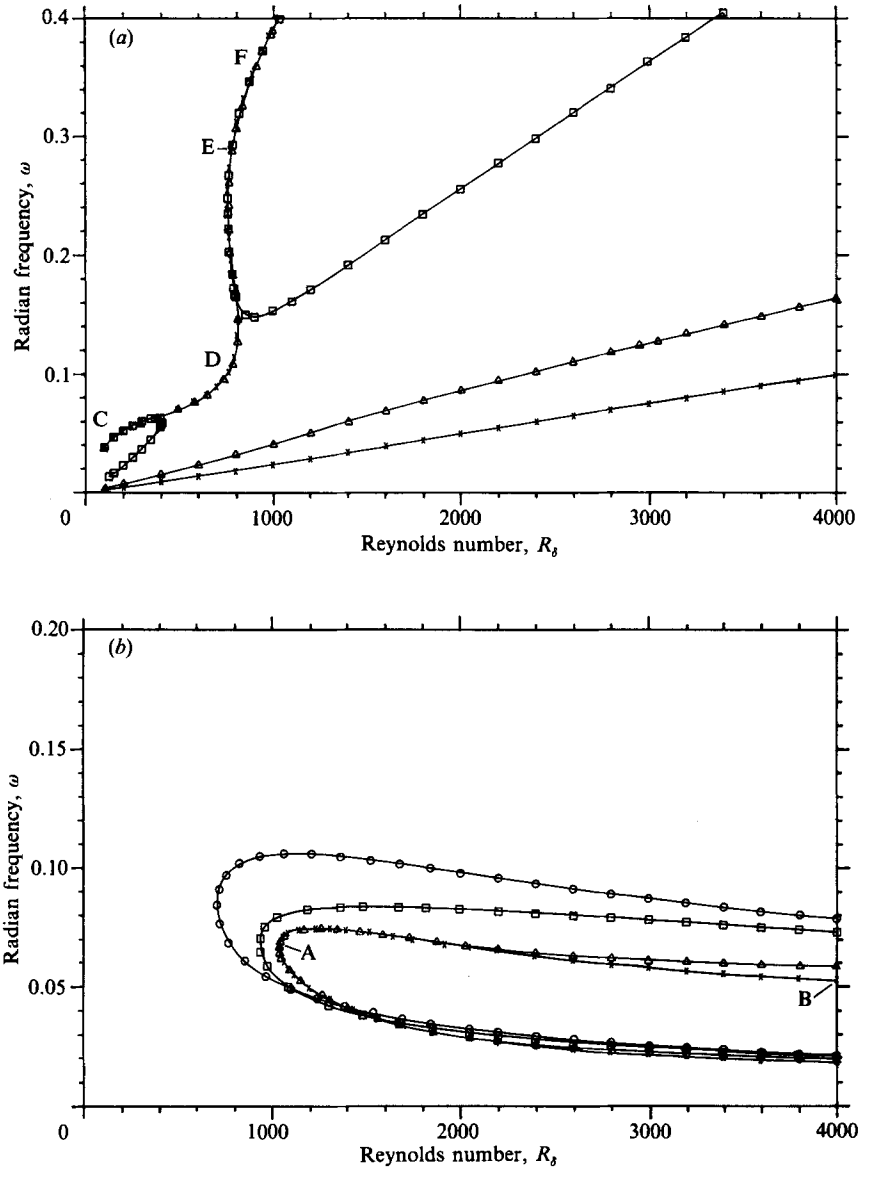

FIGURE 10. Effects of layer thickness h on the marginal stability curves for a layer with $C_t = 0.7$, $d = 0.0049$ and $K = 500$. (*a*) CIFI, (*b*) TSI. ○, $h = 0.4$; □, $h = 1.0$; △, $h = 3.0$; ×, $h = 5.0$.

amplification rates at larger R_δ up to fairly large values of h, its influence on the critical Reynolds number R_δ^{cr} is only limited to the lower values of h. Similar behaviour is to be seen in figure 7 for the material with $C_t = 1.0$. In this instance, the maximum R_δ^{cr} of about 642 is for all practical purposes achieved for a value of h between 1.0 and 2.0.

This behaviour may be qualitatively explained by appealing to equation (2.11*b*) where we note that the decay rate of a shear wave disturbance into the compliant wall is determined by the exponent b_T (which is normally smaller than b_L). Restricting ourselves to the neutral states, b_T normally increases with α_w (the wavenumber in the reference scale $L_w^{(d)}$) and C_t. Although b_T has dependence on the

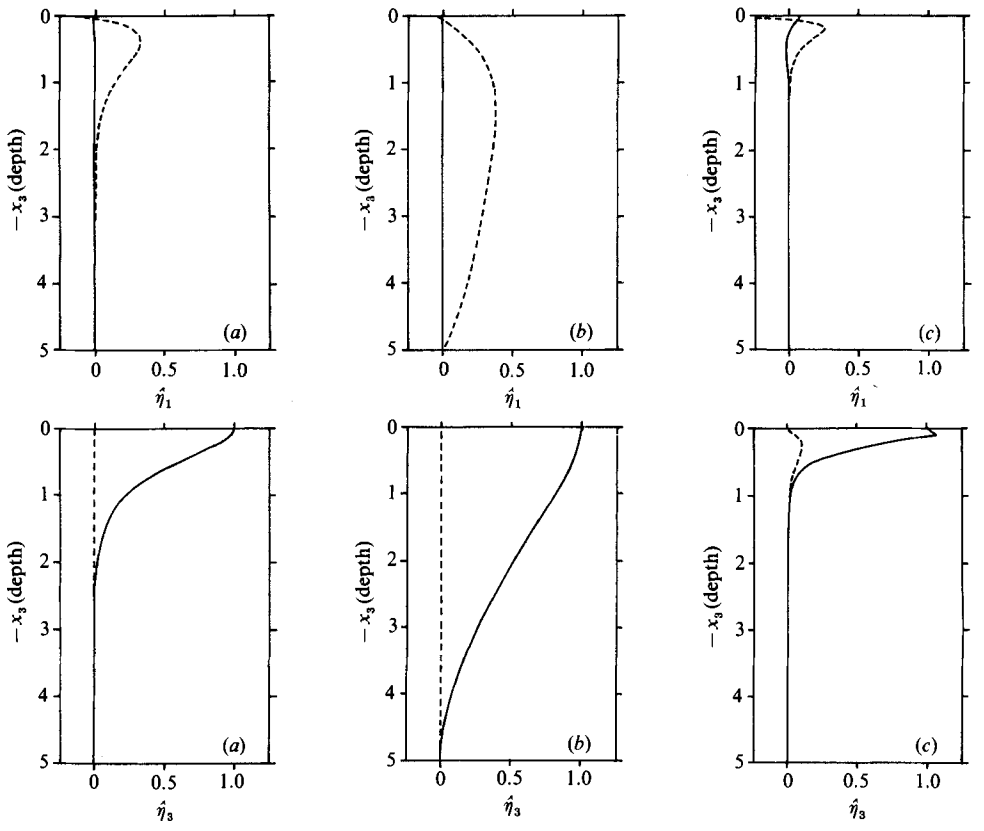

FIGURE 11. Wall eigenfunctions for the compliant wall of figure 10 with $h = 5$. (*a*) Eigenstate A. (*b*) Eigenstate B. (*c*) Eigenstate E. ——, real part; ------, imaginary part.

phase velocity c, the disturbance amplitude generally decays rapidly with the depth into the wall when α_w is large or when C_t is large; the exception being when $c > C_t$ in which case there is sinusoidal propagation into the wall with small decay. Therefore, disturbance waves of large wavenumber (short wavelength) tend to exist near the surface of the wall in a kind of skin-effect, and hard walls (with high C_t) strongly resist disturbance penetration. For the wall with $h = 5.0$, $C_t = 0.7$ and $d = 0.0049$ (see figure 10), the analysis of the eigenstate at the nose of the A regime marked point A ($\alpha_w \approx 3.25$) in figure 10(*b*) shows that $(b_T)_r \approx 2.678$, which gives an amplitude reduction factor of 10^{-3} in a distance of 2.579 into the wall; about midway through the wall. In the same distance, the eigenstate on the upper branch of the neutral curve at $R_\delta = 4000$, marked B ($\alpha_w \approx 0.792$), which has $(b_T)_r \approx 0.697$, registers an amplitude reduction factor of 0.1655. This clearly explains why increase in the wall thickness has little effect on the critical Reynolds number R_δ^{cr} when h is say greater than 2.0 because the disturbance has difficulty probing the depth of the layer and is thus indifferent to the additional depth. On the other hand, at eigenstate B, the disturbance can penetrate right through to the rigid-wall base and thus is able to reap the benefit of increase in wall thickness.

A situation similar to eigenstate A occurs along the neutral curve *CDEF* in figure 10(*a*) which therefore also explains its indifference at the larger values of h. The wall wavenumber α_w along *CDEF* ranges from about 4.0 to 12.4. At the eigenstate

marked E, $\alpha_w \approx 11.70$ and $(b_T)_r \approx 4.985$ giving thus an amplitude reduction factor of 10^{-3} in a distance of just 1.386 or 27.7% of the layer's thickness.

These analyses are confirmed by the displacement eigenfunctions for the neutral eigenstates A, B and E given in figure 11. At the eigenstate A, the horizontal and vertical displacements of the disturbance are in the main confined to a depth of 2.0 from the surface. At the eigenstate E, the skin-effect is even stronger and most of the perturbation is restricted to a depth of less than 1.0. For eigenstate B, the disturbance permeates the entire layer.

When $c > C_t$, b_T has a small real part and a relatively larger imaginary part indicating that there is sinusoidal propagation into the wall with small decay. This typically happens on the lower neutral boundaries of the unstable Class B regimes shown in figure 10(*a*). In such cases, we can expect the effect of thickness h to be very pronounced and this is quite evident in figure 10(*a*).

If the primary objective is to eliminate the CIFI, in particular the unstable B_1 regime, it is noted (figure 7) that the use of lightly damped material with $C_t = 1$ should be adequate. In the limit of vanishingly small damping, however, the proper criterion appears to be $c_R > 1$ (Yeo 1986); where c_R is the Rayleigh surface-wave speed, which is the lowest surface-wave speed that a single-layer wall can support. For an incompressible material this is equivalent to $C_t > 1.0468$.

4.3. *The effects of material damping (single-layer)*

The effects of material damping on Class A and Class B waves are well known. In fact, the response of the unstable waves to damping provides a convenient basis for classifying the unstable waves.

Figure 12 shows the effects of increasing the material damping coefficient d on the unstable Class A and Class B waves for a layer with thickness $h = 1.0$ and $C_t = 0.7$. Damping can be seen to have a beneficial effect on the B_1 regime, which can be completely suppressed even at relatively low levels of material damping. For all the levels of material damping shown, the maximum loss angles on the B_1 neutral boundaries are all less than 5°. Damping also has a strong suppressive influence on the unstable B_2 waves. There are no unstable B_1 modes at $d = 0.0147$ in the R_δ, ω range shown and the tiny remnant of the B_2 regime may be ignored. Material damping has an adverse effect on the Class A TSI regime. But for the level of damping required to eliminate the unstable Class B waves, the effect on the A regime is not dramatic (see figure 12*b*). While there is a noticeable reduction of about 200 in the critical Reynolds number R_δ^{cr} for the unstable Class A regime when the damping is trebled from $d = 0.0049$ to 0.0147, the ω-bandwidth of the regime in the higher R_δ range is hardly affected. As a result the local growth rates at the higher Reynolds numbers suffer only very small increases. The streamwise Reynolds number at which the maximum amplification factor reaches $e^{8.3}$ is about 4.438×10^6 ($R_\delta \approx 3625$), only slightly lower than the value of about 4.475×10^6 for the Class A maximum amplification envelope ($d = 0.0049$) shown in figure 6. This disproportionate influence of wall damping on the Class A TSI and the Class B CIFI was also noted by Carpenter & Garrad (1985) in their investigation of spring-backed plates. With the effective suppression of the Class B CIFI through wall damping, there is an increase in the transition Reynolds number R_δ^{tr} of about 56% over the rigid-wall value.

The effect of material damping for a much thicker wall $h = 5.0$ and $C_t = 0.7$ is shown in figure 13. A higher level of material damping is now required to suppress the unstable B_1 regime. For $d = 0.0245$, a small remain of the B_1 regime is still

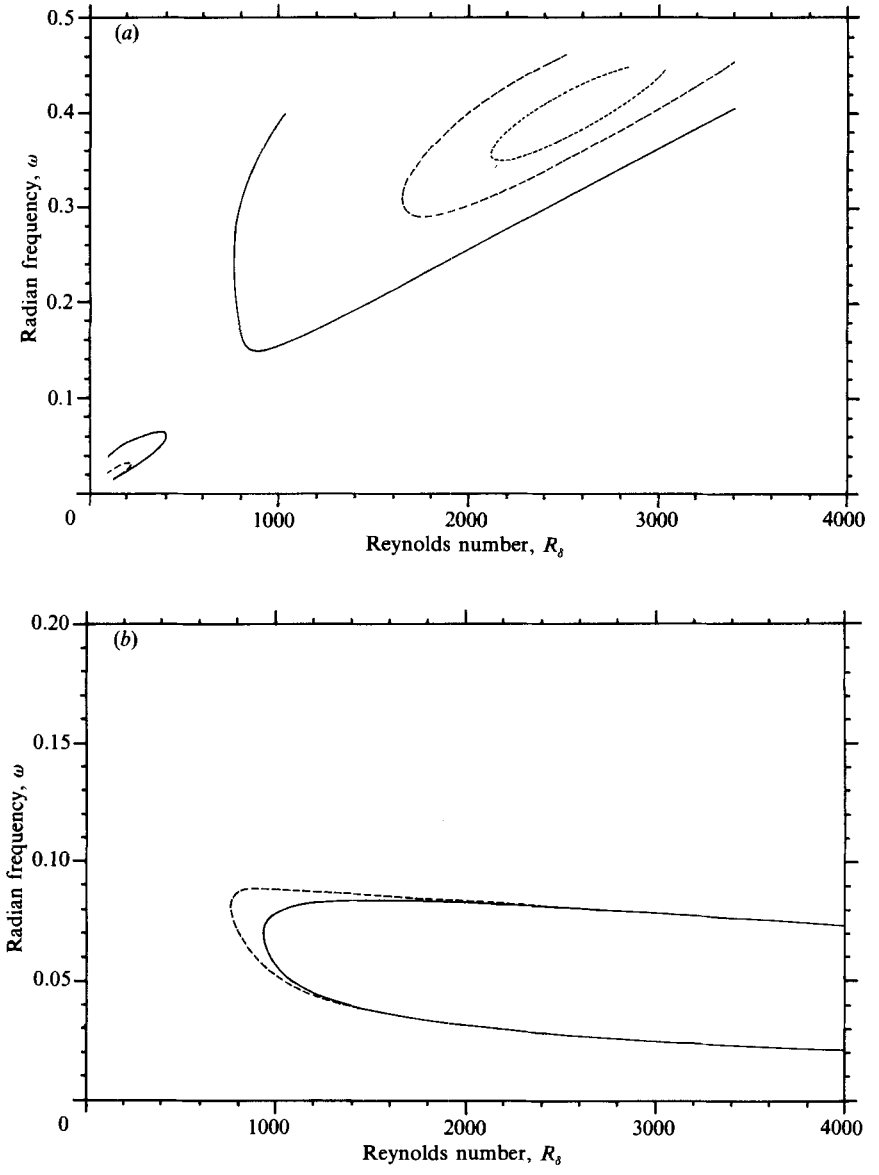

FIGURE 12. The effects of material damping on the marginal stability curves for a layer with $C_t = 0.7$, $h = 1$ and $K = 500$. (*a*) CIFI. ——, $d = 0.0049$; – – – –, $d = 0.0098$; ------, $d = 0.011$. (*b*) TSI. ——, $d = 0.0049$; – – – –, $d = 0.0147$.

present below $R_\delta = 4000$, having a R_δ^{cr} of about 3920. A small increase in d is, however, sufficient to remove the regime beyond $R_\delta = 4000$. The unstable A regimes at the two levels of damping $d = 0.0294$ and $d = 0.0588$ are shown. In both cases, the unstable B_1 regimes, if they exist, should be present only at R_δ significantly higher than 4000. For a damping coefficient $d = 0.0294$, the R_δ^{cr} for the Class A TSI regime is down to around 232, lower than the rigid-wall value of 519.06. Further enhancement of damping from $d = 0.0294$ to 0.0588 produces a significant broadening of the unstable zone at the lower-Reynolds-number end where the dimensional frequencies are higher. But this has little effect on the critical Reynolds

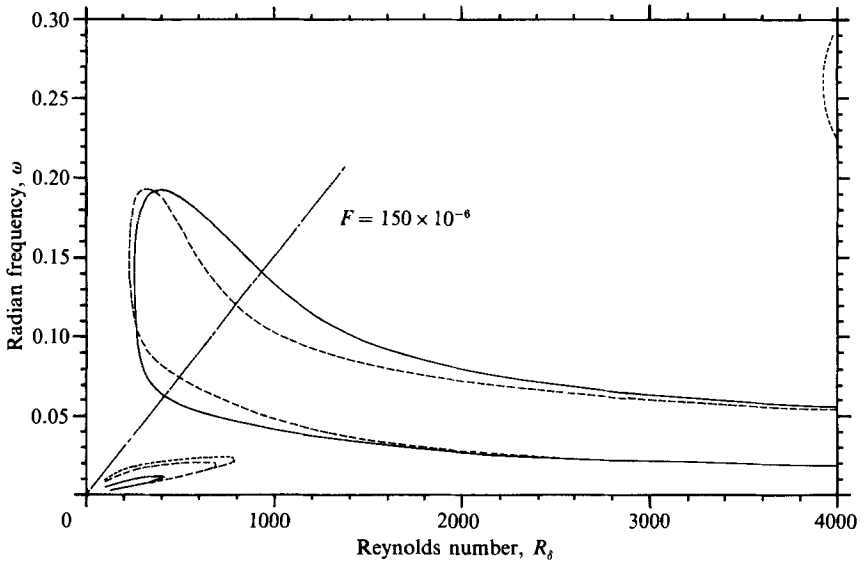

FIGURE 13. The effects of material damping on the marginal stability curves for a layer with $h = 5$, $C_t = 0.7$ and $K = 500$. ——, $d = 0.0588$; – – – –, $d = 0.0294$; ------, $d = 0.0245$.

number; in fact causing it to rise very slightly. Again, the destabilizing influence of material damping is small at higher Reynolds numbers. At $R_\delta = 4000$, the increase in the ω-bandwidth of the A regime is comparatively small for the large increase in the damping coefficient d; compare figure 10(*b*) for $d = 0.0049$ and figure 13. The local amplification rates at $R_\delta = 4000$ for the case of $d = 0.0588$ is shown in figure 9 where it may be compared against a similar wall with $d = 0.0049$ and the rigid-wall values. The increase of more than ten-fold in the damping coefficient d has produced a noticeable, but relatively small increase in the local amplification rates and the maximum amplification rate is only about 40% that of the rigid wall and 50% that of the thinner wall with $h = 1.0$. A maximum amplification of $e^{8.3}$ is obtained at $R_\delta \approx 5800$. The corresponding streamwise Reynolds number R_x is about 11.36×10^6, representing an increase of around 300% over the rigid wall's streamwise transition Reynolds number R_x^{tr} of 2.84×10^6. Transition Reynolds numbers R_x^{tr} or R_δ^{tr} of similar order to the present one have been obtained by Carpenter & Garrad (1985) for their model of the Kramer-type walls based on a transition amplification factor of $e^{9.5}$. However, it is not clear if the Class B CIFI are likely to be important in some of their cases that showed best promise. Similar and higher transition Reynolds numbers were obtained by Gyorgyfalvy (1967) in his parametric study of the theoretical transition delaying capabilities of spring-backed membranes.

The very mild destabilizing influence of the damping coefficient d on the unstable Class A TSI regime at high R_δ is believed to be largely a consequence of the very low frequency of its constituent modes. When ω_w (in the length of $L_w^{(d)}$) is small, the loss tangent $(\omega_w d)/(\rho C_t^2)$, which is a measure of the ratio of the energy lost per cycle to the maximum stored energy, increases at a slow rate with respect to increase in d. In fact, the local rate of energy dissipation in the wall is proportional to ω_w^2 according to (2.36).

Thus, for a material with $C_t = 0.7$, damping has been found to be effective in suppressing the unstable Class B waves. While there may be significant reduction in the critical Reynolds numbers for the A regime at high damping levels, the increase

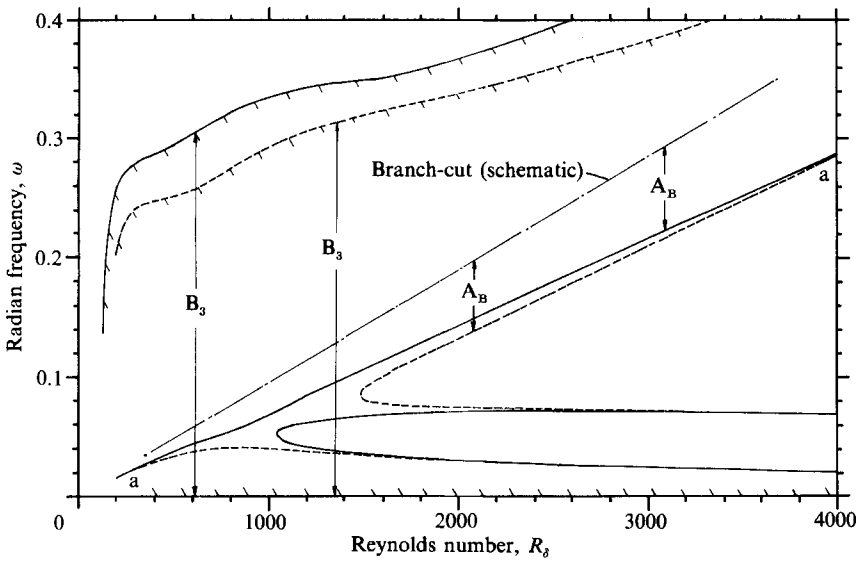

FIGURE 14. The effects of material damping on the marginal stability curves for a layer with $h = 1$, $C_t = 0.5$ and $K = 500$. ——, $d = 0.0125$; – – – –, $d = 0.0250$.

in the local amplification rates is generally small at the higher Reynolds numbers where the frequencies are low. Application of the $e^{8.3}$ transition rule seems to indicate that substantial delay in transition could be attainable. This promising delay in transition depends on two crucial factors; the choice of a sufficiently thick layer to give good Class A stability performance at higher R_δ and the suppression of the unstable Class B regimes through material damping. Since the Class A TSI regime becomes weaker at lower values of C_t and exists at lower frequencies (which suggests that they may be less affected by increase in damping), it is natural to find out if damping could also be applied to obtain improved stability performance for walls with lower C_t, such as 0.5. Unfortunately, this does not appear to be so and the effects of damping for walls with low C_t turn out to be rather complex.

Figure 14 shows the effects of material damping for a layer with $h = 1.0$ and $C_t = 0.5$. Damping can be seen to have a stabilizing influence on the unstable Class B_3 regimes causing the upper neutral boundaries to shift downwards and resulting in the contraction of the regimes and their local growth rates. The unstable B_3 regimes, however, continue to stretch to near-zero frequency and this is not at all surprising because at such low frequencies, an increase in the damping coefficient d has almost no effect on the instability. Figure 14 also shows the effects of damping on the unstable A_B regimes; the upper neutral boundaries cannot be accurately ascertained because of the branch-cut behaviour which was described in §4.2 and are thus only schematically indicated. An increase in damping is generally found to have a destabilizing influence on the unstable A_B regimes, causing the lower neutral boundaries to extend downwards to lower frequencies. It is primarily because of this destabilizing response that it was decided earlier on to label the instability A_B. The subscript B is appended to highlight the link it seems to have with Class B instability. For if we are to increase the value of C_t at a given R_δ and hold the other wall parameters constant, the lower boundary, a–a for example, can be shown to be continuously connected to the lower neutral boundary of the unstable Class B_1 regimes at higher values of C_t, say 0.7.

The A_B regime is also a compliance-induced instability. Comparison of figures 8 and 14 shows that the unstable A and A_B regimes approach each other as the damping coefficient d is increased. The two regimes coalesce at a value of d between 0.0125 and 0.0250. The extent of the coalescence grows with further increase in the level of damping. Broadly similar trends are also observed for the layer thickness of $h = 5.0$. For this wall thickness, the coalescence or merging of the A and the A_B regimes sets in at a higher value of d, between 0.0294 and 0.0392.

The occurrence of coalescing unstable modes had been reported by Carpenter, Gaster & Willis (1983) for boundary-layer flow over compliant walls modelled as spring-backed bending plate with viscous substrate. The coalescence between a TSI and a CIFI regimes was brought about by increase in substrate viscosity. Coalescence between TSI and CIFI, of a slightly different kind, was also observed by Gyorgyfalvy (1967) in his study of spring-backed membrane. In his case, the coalescence was brought about by reduction in the foundation stiffness. He named it a Class C divergence instability and attributed its occurrence to the coincidence or the near-coincidence of the wave velocity of the surface and maximum phase speed of the TSI waves. In our case, it is noted that the lowest free-wave velocity c_R (ignoring dissipation) of the walls with $C_t = 0.5$ is approximately 0.478. This is within close range of the maximum TSI phase speed.

The stability characteristics of flows over single-layer walls of low C_t, such as 0.5, are exceedingly complex and the above results are necessarily incomplete. What is certain, however, is that such low C_t walls suffer from strong instabilities, and increase in the material damping coefficient d is not an effective measure to improve the stability performance. An increase in the damping level leads to a coalescence between the Class A TSI and the A_B (CIFI) regimes. These effectively put a limit on the softness of the materials that can be used for single-layer compliant walls if strong CIFI are to be avoided.

4.4. *Material compressibility (single-layer)*

The effects of material compressibility have seldom been examined. Available results are in the main devoted to nearly incompressible materials because solid rubber-based materials have generally been assumed to be the type of material suitable for the construction of compliant walls. With advances in material processing technology this may no longer be true.

Material compressibility can be important if, for example, porous materials or materials containing a uniform distribution of voids are used. The porous materials or the voids could be saturated or partially filled in with a viscous fluid to provide a measure of control over the damping characteristics of the wall similar to the original Kramer walls. If the local variations of the properties and states occur on a lengthscale that is much shorter than the disturbance lengthscales, some form of average properties can be defined. This would allow a macroscopic treatment of the complex dynamics. For single-layer walls, it is necessary of course to assume that the flow–wall interface is smooth and impermeable to the external flow.

When the compressional wave speed c_L is significantly larger than C_t, the compliant response of the layer is largely determined by the latter. The effect of reducing c_L, other things being equal, is to make the wall more compliant. The effects on stability are, however, only significant when c_L approaches the order of C_t. Figure 15 shows these effects for a wall with $h = 3.0$, $C_t = 0.8$ and $d = 0.0049$. At $K = 1.067$ (or $c_L \approx 1.386$), there is a large improvement in the unstable A regime both in terms of an increase in the critical R_δ and a sizeable all round decrease in the ω-bandwidth.

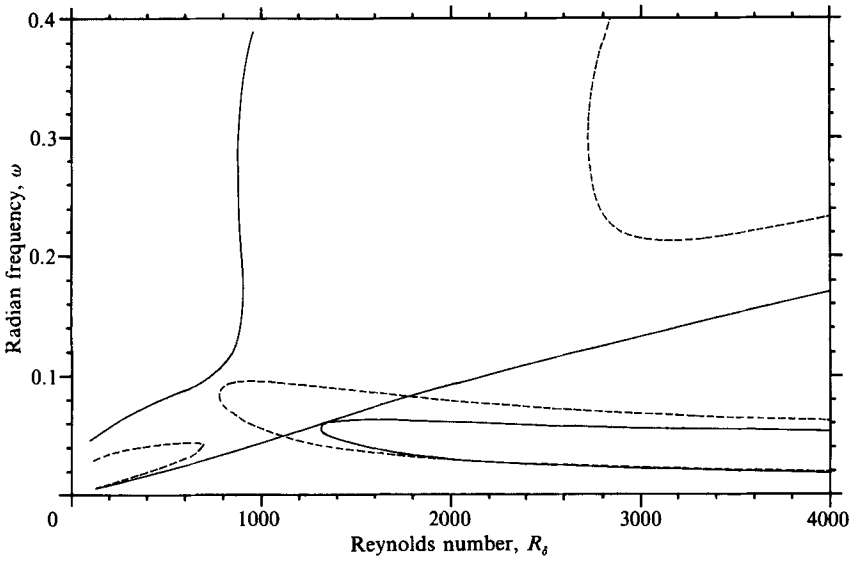

FIGURE 15. The effects of material compressibility on the marginal stability curves for a layer with $h = 3$, $C_t = 0.8$ and $d = 0.0049$. ——, $K = 1.067$; – – – –, $K = 500$.

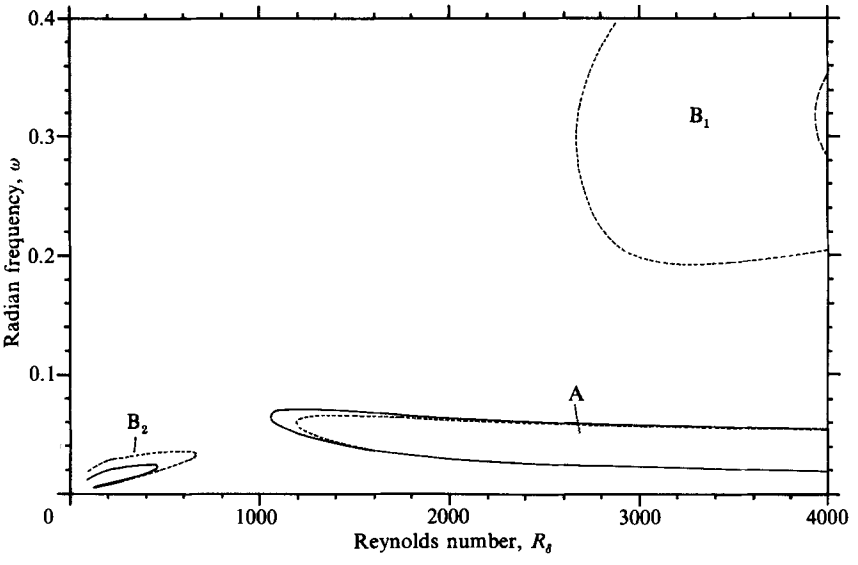

FIGURE 16. The effects of material damping on the marginal stability curves for a compressible layer with $h = 3.0$, $C_t = 0.8$ and $K = 1.067$. ——, $d = 0.0245$; – – – –, $d = 0.02156$; – – – –, $d = 0.0147$.

As we have come to expect, there is a concomitant escalation of the unstable B_1 and B_2 regimes which merge to form a large Class B regime that extends over the full range of R_δ shown. Unless this Class B regime can be effectively suppressed, there is no gain in stability. Figure 16 shows the effects of material damping on the marginal stability curves of the highly compressible wall in figure 15. It is observed that increase in damping has a very strong stabilizing influence on the unstable Class B regimes; inducing its bifurcation into the B_1 and the B_2 regimes and the progressive retreat of the unstable B_1 regime to higher Reynolds numbers R_δ. A four-fold increase

in damping from $d = 0.0049$ (figure 15) to $d = 0.0245$ is sufficient to remove the unstable B_1 regime to R_δ higher than 4000. The remaining B_2 regime may be ignored.

Comparison of figures 15 and 16 reveals that damping has only a small detrimental effect on the unstable A regime. The increase in damping from $d = 0.0049$ to 0.0245 produces a fairly noticeable reduction in the R_δ^{cr}, but otherwise, not affecting the ω-bandwidth or the local amplification rates in any significant manner. A maximum amplification factor of $e^{8.3}$ is reached at $R_\delta \approx 5800$ ($R_x^{tr} \approx 11.36 \times 10^6$). The transition R_x achieved for this wall is about the same as that attained using a thicker layer ($h = 5.0$) of a nearly incompressible material with lower $C_t = 0.7$ (figure 13); damping being used in both cases to suppress the CIFI. The compressible case, despite its smaller thickness and higher C_t, however, has greatly improved TS stability in the lower half of the R_δ range.

Thus material compressibility can have the potentially beneficial influence of delaying transition. The role played by material damping in the effective suppression of the Class B CIFI is again very crucial.

5. Multi-layer viscoelastic walls

The studies of the preceding sections help to identify the kinds of walls that show potential for substantial transition delay as well as those which are likely to have disastrous effects on flow stability. The investigation is extended to multi-layer cases here. To keep the task manageable, only two main categories of multi-layer walls are examined below.

The first category consists mainly of two-layer walls in which the first layer is a thin layer of a stiff material and the second layer is a thick layer of softer material. The attachment of a thin layer of stiff material onto a highly compliant layer is usually highly desirable in practice because it helps to protect the underlying soft layer from accidental damage. The second category has been chosen to be a class of four-layer walls which have relative layer thicknesses similar to the complex multi-layer walls designed by Kramer (1960). The material properties in the latter category are selected to give the walls good potential for delaying transition. For the case of two-layer walls, attention is focused mainly on how the parameters of the top layer affect the instabilities. For this purpose the elastic shear speed and the damping coefficient of the material for the second layer is fixed at $C_t^{(2)} = 0.7$ and $d^{(2)} = 0.0049$ respectively to facilitate comparison with the single-layer results of the preceding section. The superscript (j) denotes the jth layer. A very short study is also made of the stability consequences of placing the stiffer thin layer in an alternative position embedded within the softer layer.

As in the preceding section, the densities of the materials are all selected to be 1.0. All the wall properties are given in the reference scales of the walls for $R_w = 2 \times 10^4$.

5.1. *The effects of top-layer $C_t^{(1)}$ and $h^{(1)}$ (two-layer)*

Figure 17 shows the effects an increase in the material stiffness of the top layer has on the marginal stability curves of a two-layer wall having an overall thickness of $h = 1.0$. The thickness of the top layer is $h^{(1)} = 0.05$. An increase in C_t anywhere in a compliant wall generally renders the wall less compliant, and qualitatively we can expect the TSI to be destabilized and the CIFI to be stabilized. These effects are clearly reflected in the figure. More significantly, however, it may be noted that the stabilizing influence of increase in $C_t^{(1)}$ on the unstable B_1 regimes is much stronger

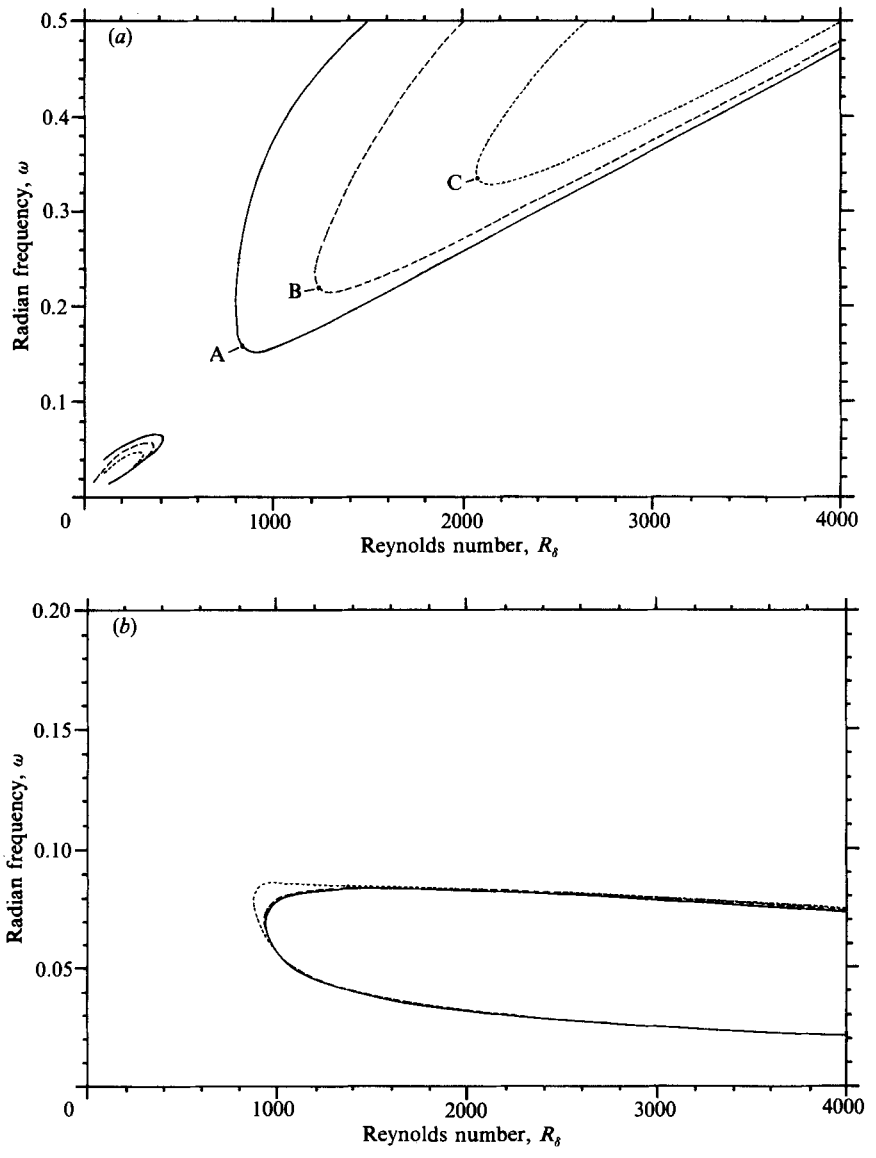

FIGURE 17. The effects of top-layer C_t on the marginal stability curves of a two-layer wall. Layer 1: $h = 0.05, d = 0.0000, K = 1200$. Layer 2: $h = 0.95, d = 0.0049, K = 500, C_t = 0.7$. (*a*) CIFI. (*b*) TSI. ——, $C_t^{(1)} = 1.0$; – – – –, $C_t^{(1)} = 3.0$; ------, $C_t^{(1)} = 6$.

than its destabilizing influence on the unstable A regimes. The stabilizing influence on the B_2 regimes is also comparatively mild. An increase in $C_t^{(1)}$ from 1.0 to 6.0 produces a reduction in the R_δ^{cr} of the unstable A regime of less than 100. There is an increase in the ω-bandwidth but this does not appear to be unduly serious. The same increase in $C_t^{(1)}$ results in a rapid retreat of the unstable B_1 regime yielding an increase in the R_δ^{cr} of around 1100. Much of this increase is attributed to the movement of the upper branch of the neutral boundary to higher R_δ. There is relatively less movement on the lower neutral boundary. A sizeable unstable B_1 regime remains at $C_t^{(1)} = 6.0$, but this could be suppressed by further increase in $C_t^{(1)}$, with some attendant detrimental effect for the A regime.

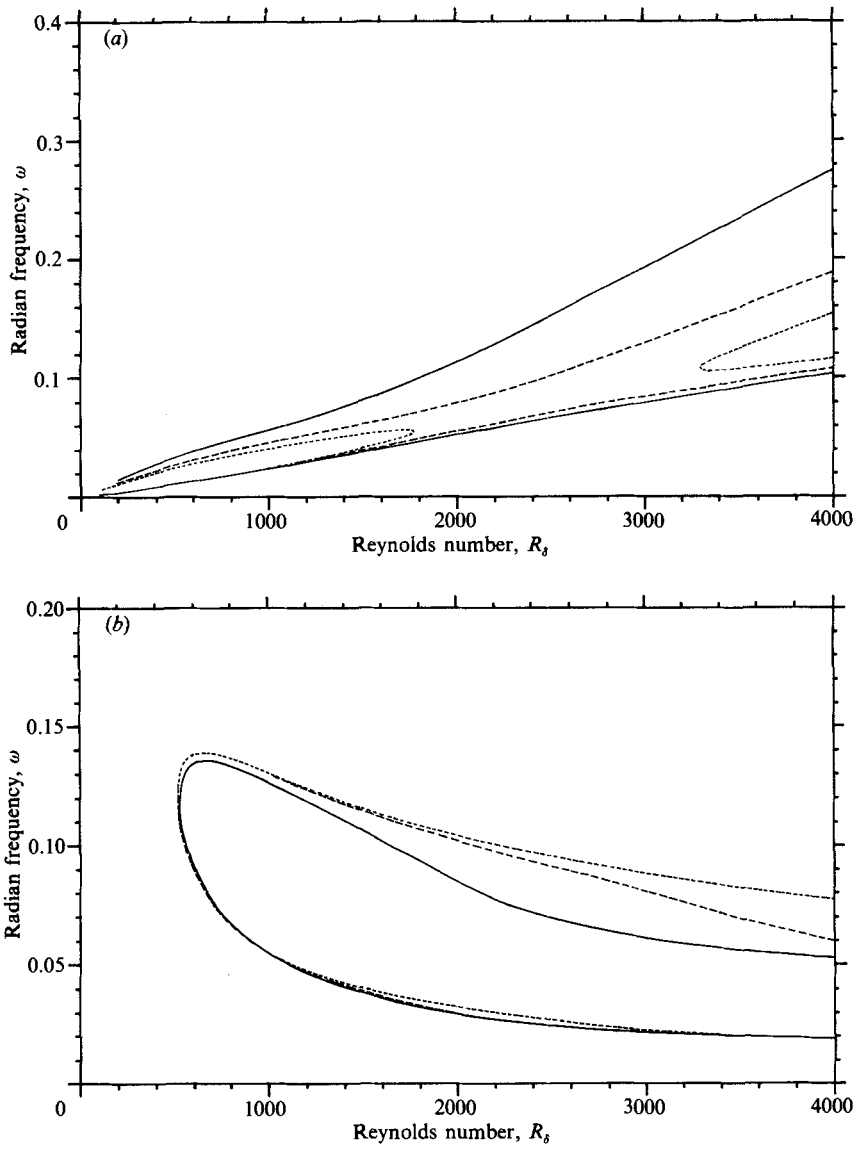

FIGURE 18. The effects of top-layer C_t on the marginal stability curves of a two-layer wall. Layer 1: $h = 0.25$, $d = 0.0049$, $K = 1200$. Layer 2: $h = 4.75$, $d = 0.0049$, $K = 500$, $C_t = 0.7$. (*a*) CIFI. ——, $C_t^{(1)} = 3.0$; – – – –, $C_t^{(1)} = 6$; - - - - -, $C_t^{(1)} = 8$. (*b*) TSI. ——, $C_t^{(1)} = 3$; – – – –, $C_t^{(1)} = 9$; - - - - -, $C_t^{(1)} = 30$ ($K = 4050$).

We next consider the effects of the top-layer $C_t^{(1)}$ for a much thicker two-layer wall; $h^{(1)} = 0.25$ and $h^{(2)} = 4.75$. It is very evident from a comparison of figure 18 and the marginal curves for the single-layer wall with $h = 5.0$ in figure 10 that an increase in $C_t^{(1)}$ brings about relatively small improvement to the lower neutral boundary of the unstable B regime. The corresponding effect of an increase in $C_t^{(1)}$ on the upper neutral boundary (CDEF in figure 10*a*) is very much stronger. Increase of $C_t^{(1)}$ from 0.7 (single-layer case) to 3.0 is sufficient to reduce the unstable B regime to a narrow frequency wedge. Further increase in $C_t^{(1)}$ produces further narrowing of this wedge, resulting mainly from the downward movement of the upper neutral boundary, and

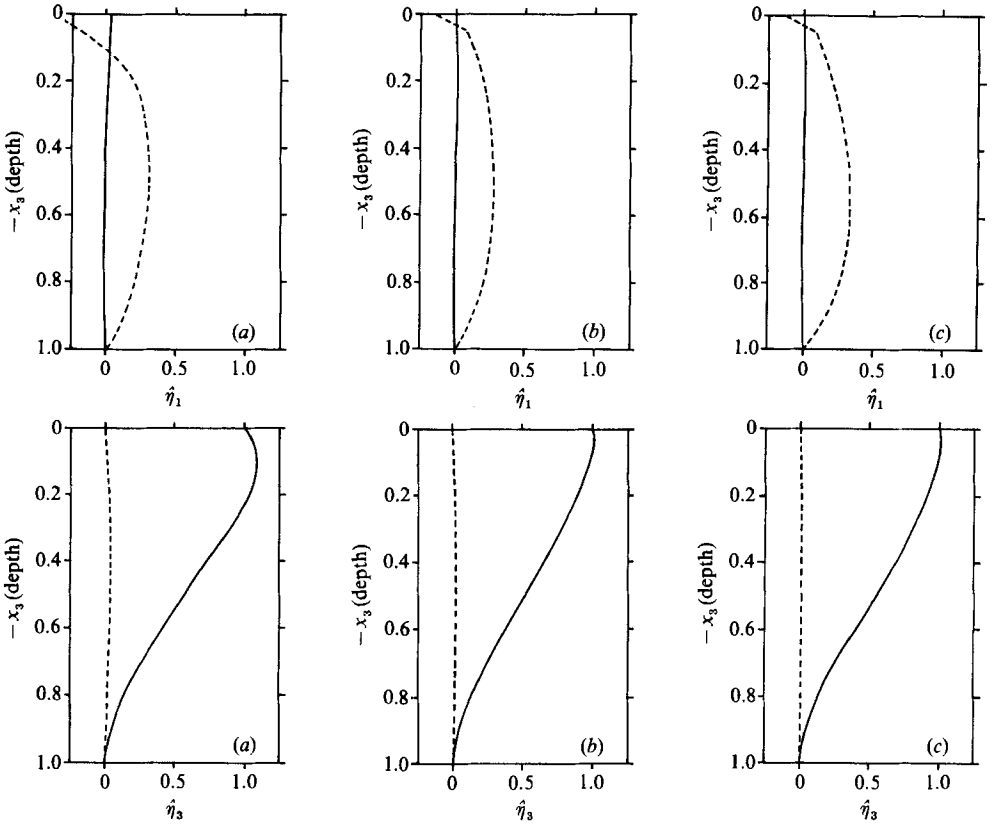

FIGURE 19. Wall eigenfunctions at the nose of the B_1 regime for two-layer walls having different top-layer C_t in figure 17(*a*). (*a*) Eigenstate A, $C_t^{(1)} = C_t^{(2)} = 0.7$. (*b*) Eigenstate B, $C_t^{(1)} = 3$. (*c*) Eigenstate C, $C_t^{(1)} = 6$. ——, real part; ------, imaginary part.

a subsequent bifurcation into the unstable B_1 and B_2 regimes. The unstable B_1 retreats beyond $R_\delta = 4000$ at $C_t^{(1)} = 9.0$. At $C_t^{(1)} = 8.0$, the maximum R_δ for the B_2 regime is high at $R_\delta \approx 1775$, but its amplification rates are still very low. For the unstable A regime, an increase in $C_t^{(1)}$ from 0.7 to 3.0 quickly causes the R_δ^{cr} to fall to a value near that of the rigid wall. The increase in the ω-bandwidth at large R_δ is much less significant. For $C_t^{(1)}$ between 3.0 and 9.0, a prominent broadening of the ω-bandwidth of the unstable A regime occurs signifying an increase in the local amplification rates. At a high elastic shear speed $C_t^{(1)} = 30.0$, the entire A regime is very close to that of the rigid wall.

As in §4, it is found that a fairly coherent explanation of the changes in the stability characteristics of the walls may be obtained from the analysis of the wall eigenfunctions. Figure 19 shows the wall eigenfunctions for the neutral eigenstates near the 'noses' of the B_1 regimes for the thinner two-layer walls (overall $h = 1.0$, figure 17*a*). The displacement eigenfunctions of the top layer in figure 19*b*, *c* display distinctively plate-like behaviour; with an anti-symmetrical type of oscillational mode. Distinct differences exist between these and the eigenfunctions for $C_t^{(1)} = 0.7$ given in figure 19(*a*). In the latter case, the magnitude of the horizontal displacement η_1 at the surface (subject to the normalization $|\eta_3| = 1$) is significantly larger than the other two cases. This is greatly reduced at $C_t^{(1)} = 3.0$ and 6.0 to that which results mainly from the oscillations of the 'plate'. Horizontal stretching in the vicinity of

the surface is also strongly resisted by the stiff top layer (compare the amount of horizontal displacement at the position of the neutral axis of the 'plate' in the three cases). This resistance to stretching is to be expected from the greater stiffness of the top layer.

Detailed study of the wall eigenfunctions shows that, in general, the top layer assumes a plate-like response when it is materially stiffer than the second layer. The larger the ratio of shear speeds $C_t^{(1)}/C_t^{(2)}$, the stronger the plate-like behaviour. For small displacement amplitude and small plate-layer thickness $h^{(1)}$ relative to the disturbance wavelength, the dynamic response of the top layer may be approximated by that of the bending plate. This assumption is implicit in the compliant wall model used by Carpenter *et al.* The bending-plate model which they had used would only be good if the material stiffness of the top layer is significantly higher than the stiffness of the elastic foundation; otherwise, a elastic or viscoelastic layer model would be more appropriate.

Given the plate-like response of the top layer when $C_t^{(1)}/C_t^{(2)}$ is large, the influence of the top layer on the stability may to a large extent be deduced from the governing equation for a bending plate:

$$\rho^{(1)}h^{(1)}\frac{\partial^2\eta_3}{\partial t^2}+B\frac{\partial^4\eta_3}{\partial x_1^4}=\sigma_{33}, \tag{5.1}$$

where $B=E(h^{(1)})^3/12(1-\nu^2)$ is the flexural rigidity of the 'plate'; $E=2\rho^{(1)}[C_t^{(1)}]^2(1+\nu)$ is the Young's modulus, ν is the Poisson's ratio and σ_{33} is the net vertical stress acting on the plate layer. The impedance of the 'plate' is then proportional to

$$\frac{\rho^{(1)}h^{(1)}\alpha_w}{c}(C_\alpha^2-c^2), \tag{5.2}$$

where $C_\alpha=\alpha_w h^{(1)}C_t^{(1)}/3^{\frac{1}{2}}$ is the free-bending wave speed of the plate layer. For the cases of interest considered herein, the impedance of the plate to the formation of a bending wave is largely dominated by C_α^2; c being generally within the range 0.25–1.0. For qualitative analysis, the bending impedance can be taken as a first approximation to be proportional to

$$C_t^2\alpha_w^3(h^{(1)})^3. \tag{5.3}$$

According to (5.3), the rate of increase in the impedance of the plate layer with respect to an increase in $C_t^{(1)}$ is, for a given $h^{(1)}$, proportional to α_w^3 and therefore large when α_w is large. Since the eigenstates along CDEF and at point A in figure 10 ($h=5.0$ case) have rather large α_w as noted in §4.2, the effect of any increase in $C_t^{(1)}$ on the impedance will be large. On the other hand, the α_w along the lower neutral boundary of the B regime in figure 10(*a*) are low, and therefore the effect of changes in $C_t^{(1)}$ will be proportionately smaller. This qualitatively explains the different rates of response of the lower and the upper neutral boundaries of the unstable B regime to increases in $C_t^{(1)}$ as observed in figure 18(*a*). For the A regime (see figures 18*b* and 10*b*, $h=5.0$) a similar rationale may explain the relatively stronger effect of an increase in $C_t^{(1)}$ on the nose region and the milder effects at large R_δ, say at 4000, when $C_t^{(1)}$ is increased from 0.7 to 3.0. The increase in $C_t^{(1)}$ from 3.0 to 30.0 has little further effect in the nose region of the A regime because the neutral boundaries there are then already close to the rigid wall's neutral boundary. At $R_\delta=4000$, there is a gradual enhancement of the ω-bandwidth as $C_t^{(1)}$ rises.

For the thinner two-layer walls (overall $h=1.0$), the same explanation applies to

what is observed in figure 17(*a*) since α_w is larger on the upper neutral boundaries than on the lower ones for the B_1 regimes. The smaller reduction in the critical Reynolds number R_δ^{cr} of the unstable A regime shown in figure 17(*b*) as compared with the much greater reduction for the thicker two-layer wall (from $C_t = 0.7$ in figure 10*b* to $C_t = 3.0$ in figure 18*b*) can be explained by taking into account the dependence of the impedance on $h^{(1)}$. Since $h^{(1)}$ for the thicker wall is 5 times the $h^{(1)}$ for the thinner wall, the rate of increase in the impedance of the top layer with respect to $C_t^{(1)}$ is 125 times as high for the same α_w. This explains the rapid reduction in the R_δ^{cr} for the thicker wall when $C_t^{(1)}$ is varied from 0.7 to 3.0. For both the thinner and the thicker walls considered, the effects of $C_t^{(1)}$ variation on the B_2 regime (or the low-R_δ end of the merged B_1 and B_2 regime) is comparatively small because of the low values of α_w. Here C_α may also be of the order of the phase speed c.

To obtain improvement in overall stability, it is frequently necessary to adjust $C_t^{(1)}$ and $h^{(1)}$ in opposite directions such that there is minimal adverse influence on the A or TSI regime while gain in stability is achieved on the CIFI. For a top layer which behaves like a plate and for which C_α^2 is more dominant than c^2, it seems natural to hold $(C_t^{(1)})^2(h^{(1)})^3$ constant while varying $C_t^{(1)}$ and $h^{(1)}$. Other things being equal, this corresponds to bending plates having the same flexural rigidity; the free bending wave speed then varies as $1/(h^{(1)})^{\frac{1}{2}}$. Figure 20 shows the effects on the stability of varying $C_t^{(1)}$ and $h^{(1)}$ such the $(C_t^{(1)})^2(h^{(1)})^3$ is kept constant. The second layer is much thicker and softer with $h^{(2)} = 4.5$ and $C_t^{(2)} = 0.7$. It can be seen in figure 20(*b*) that the different combinations of $C_t^{(1)}$ and $h^{(1)}$ have closely identical A regimes. The reduction in $h^{(1)}$, which is accompanied by increase in $C_t^{(1)}$, has a rather mild destabilizing influence on the A regime especially at the higher R_δ where the frequencies are low. In figure 20(*a*), it is noted that the reduction in $h^{(1)}$ has a stronger stabilizing influence on the CIFI regimes. From the viewpoint of stability these results suggest that subject to $(C_t^{(1)})^2(h^{(1)})^3$ being constant, thin top layers with high $C_t^{(1)}$ are preferable to thicker ones with lower $C_t^{(1)}$. The bulk modulus of the first layer $K^{(1)}$ was varied merely as a convenient means of keeping the Poisson's ratio constant and the variation does not affect the results in any significant way.

5.2. *Other locations of the stiff layer (three-layer)*

Up to now, we have considered only cases in which the stiff layer is the top layer. While it fulfils the important practical function of protecting the softer sublayer, it would be interesting to find out if it is necessarily in the best interest of stability to place the stiff layer at the top. We consider this problem for the case of a compliant wall of overall thickness $h = 1.0$.

The marginal stability curves for three different positions of the stiff elastic layer of thickness $h = 0.05$ and $C_t = 3.0$ are given in figure 21. The three locations are

(i) stiff layer at the top,

(ii) top surface of stiff layer at a distance $s = 0.2$ from the flow–wall interface, and

(iii) top surface of stiff layer at a distance $s = 0.5$ from the flow–wall interface.

The detailed properties are given in the figures.

If the purpose is to maximize Class A stability, then clearly the thin stiff layer should be located at the top ($s = 0$). Placing the layer at $s = 0.2$ evidently has a strong destabilizing effect on the A regime near the nose; R_δ^{cr} is reduced by approximately 400. The destabilizing effect, however, recedes rather quickly as we get to higher Reynolds numbers. This implies that for the low-frequency (small $F = \omega/R_\delta$) instability waves normally associated with transition the increase in

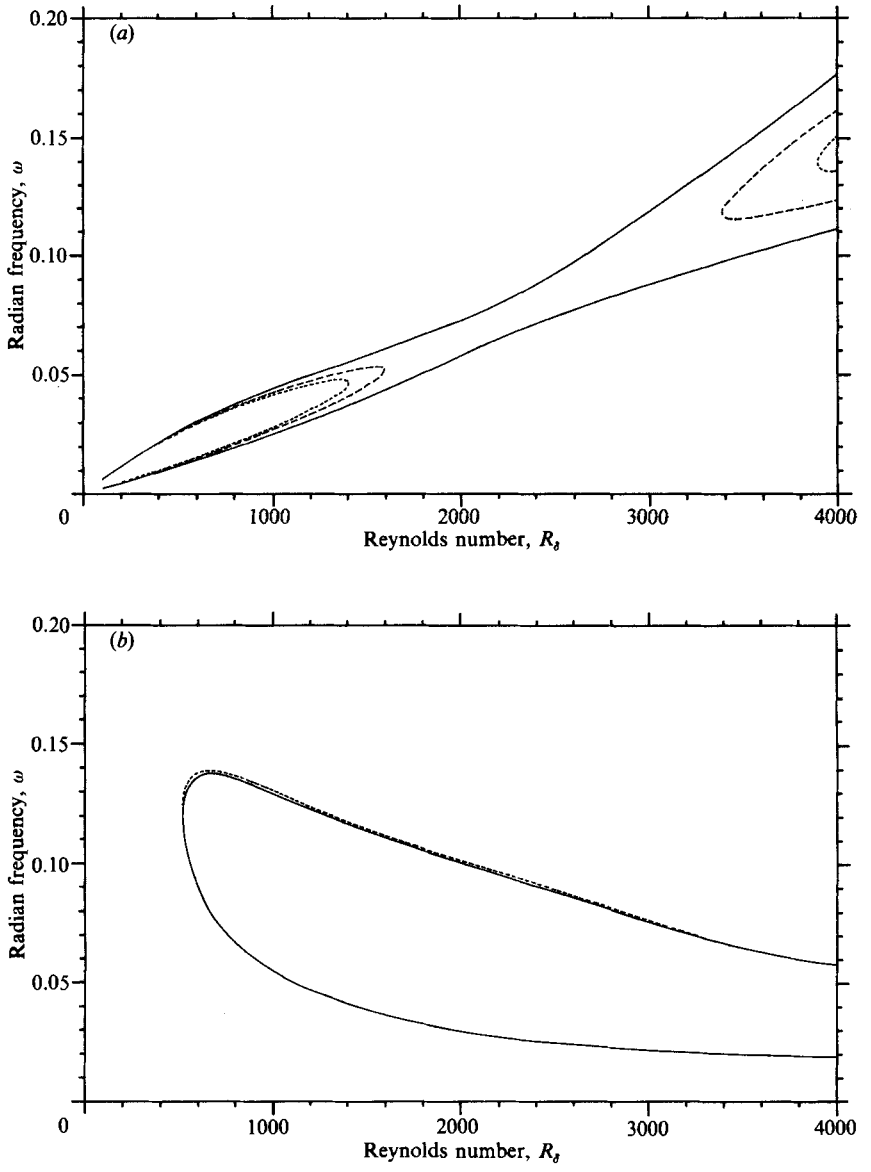

FIGURE 20. Marginal stability curves for two-layer walls having different top-layer thicknesses but the same flexural rigidity according to bending plate theory. (*a*) CIFI, (*b*) TSI. Layer 1: ——, $h = 0.4$, $C_t = 3.500$, $d = 0$, $K = 1633.3$. – – – –, $h = 0.2$, $C_t = 10.11$, $d = 0$, $K = 2008.7$. ------, $h = 0.1$, $C_t = 33.01$, $d = 0$, $K = 2360.7$. Layer 2: $h = 4.5$, $C_t = 0.700$, $d = 0.0049$, $K = 500$.

disturbance amplification would be small; the loss of Class A stability near the nose is not crucial to transition. Furthermore, placing the thin stiff layer at $s = 0.2$ produces a very strong stabilizing influence on the B regime. The improvement in B_1 stability may, in many walls, more than compensate for the small loss in low-frequency Class A stability. For walls dominated by strong B-type instabilities, placing the stiff layer at a short distance below the surface may be a good alternative to increasing wall damping as a means by which to improve the stability characteristics of the wall from the viewpoint of delaying transition.

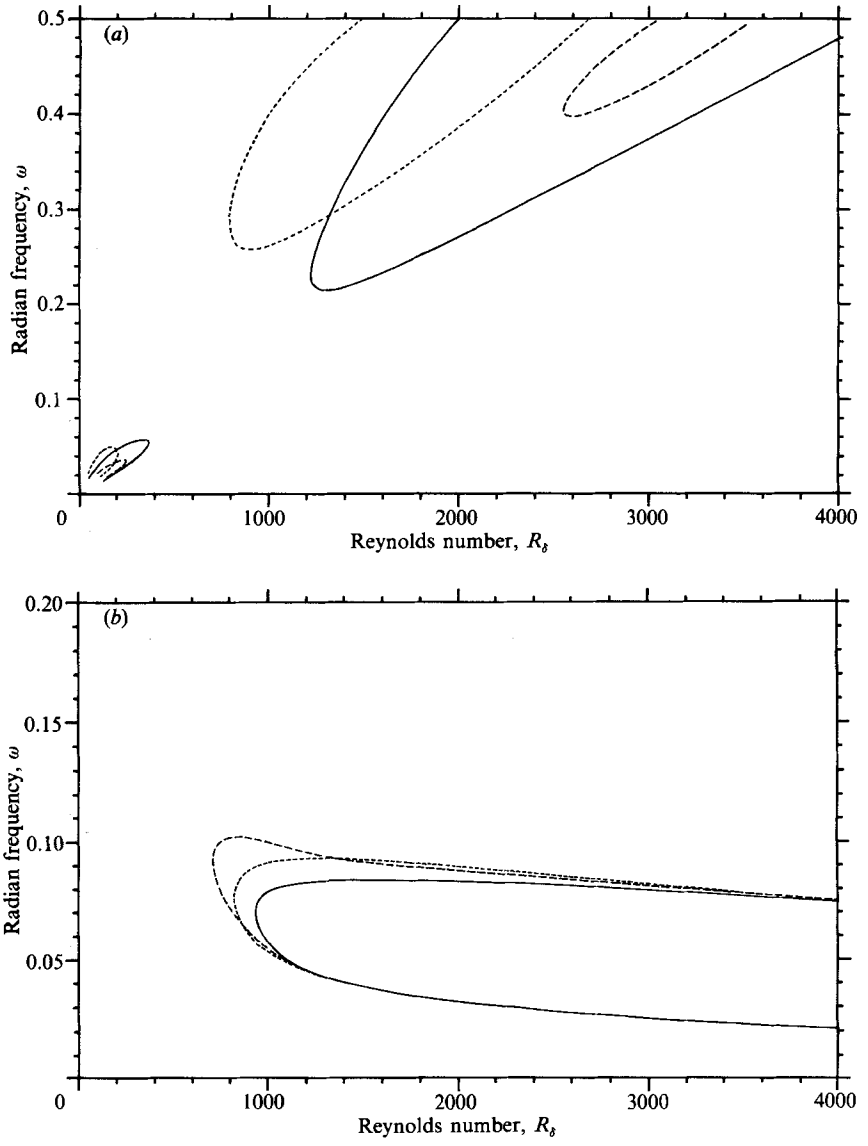

FIGURE 21. The effects of the location of the stiff layer on the marginal stability curves for a three-layer wall of overall thickness 1.0.

Material data for compliant wall:

Layer no.	h	C_t	d	K
1	s	0.7	0.0049	500
2	0.05	3.0	0.0000	1200
3	$0.95-s$	0.7	0.0049	500

(*a*) CIFI. (*b*) TSI. ——, $s = 0$; – – – –, $s = 0.2$; ------, $s = 0.5$.

5.3. *A specific class of four-layer walls*

The theoretical formulation that had been developed allows multi-layer walls to be treated in a uniform fashion. Here, we examine the stability of a class of four-layer walls which bear certain geometric similarities with the original compliant walls of Kramer (1960); in that the relative thicknesses of the layers are the same as that of

the more complex Kramer walls. It is, of course, not possible in the present treatment to simulate the periodic character of the Kramer walls and the complex dynamics associated with the sloshing of the viscous liquid substrate among the stubs. Carpenter and coworkers had attempted to model the Kramer walls as a bending plate on an elastic foundation with a viscous liquid substrate that acts independently of the foundation. The basis of their model is that for long wavelength disturbances the periodicity of the stubs can be ignored. This seems a fair assumption because the important unstable waves which are responsible for transition to turbulence tend to have wavelengths which are significantly longer than the characteristic dimensions of the boundary layer and the stub spacings. The present theoretical model requires only minor additions if it is felt desirable to superpose a viscous liquid substrate which acts independently of the layer. It is merely necessary to sum the stress contributions from the viscous substrate and the layer and to ensure that the liquid substrate satisfies the kinematic boundary conditions at the interfaces with the adjacent layers. The essential theory governing the dynamics of the liquid substrate and the interface conditions can be found in Yeo (1986). This course is not pursued here and the intention is not to attempt to justify Kramer's experimental findings because it is not certain to the author if the present model will do justice to Kramer's case. Besides, the material properties of the original Kramer walls have always been a subject of some controversy. Instead the properties of the four-layer walls were chosen, drawing upon the experience accumulated from previous runs, to give compliant walls which show greatly reduced disturbance growth rates and hence the potential for substantially delaying the transition.

The properties of the four-layer walls were selected such that the top layer consists of a fairly stiff material which has $C_t^{(1)}$ greater than or equal to the free-stream velocity. The second layer which is three times as thick as the first is of a softer material with $C_t^{(2)} = 0.8$. The material damping coefficients of these layers were set to a nominal value of $d^{(1)} = d^{(2)} = 0.0049$ (a fairly low level). This choice of damping is not crucial unless $d^{(1)}$ and $d^{(2)}$ are fairly large. Quite often, the enhancement of damping helps to suppress the CIFI without serious adverse effect on the Class A TSI waves at large Reynolds numbers R_δ. The third layer, which corresponds to Kramer's layer of stubs, was chosen to be very soft with $C_t^{(3)} = 0.4$ and the level of material damping can be varied to exercise control over the unstable CIFI, which are Class B. No special consideration was given to the choice of properties for the last layer which were set at $C_t^{(4)} = 0.8$ and $d^{(4)} = 0.0049$. The layers were assumed to be nearly incompressible with the exception of the third for which a low bulk modulus was assigned to account for the significant compressibility effect which is likely to be present in Kramer's walls. The detailed specifications of the walls will be given in the figures presented.

The choice of material properties for the top layer has been guided by the principle, demonstrated in §4.2, that the short-wavelength and high-frequency disturbances, which are mostly associated with the CIFI, tend to persist near the surface of the wall. These CIFI are effectively suppressed with the choice of relatively stiff material. The reduction of the material stiffness with the depth is designed to provide a progressively lower resistance to penetration by the longer wavelength Tollmien–Schlichting disturbance modes, thus enabling these waves to 'probe' the depth of the wall and hence to realize the full compliance of the wall to achieve maximum stabilization. Undesirable CIFI waves of longer wavelength which get through, but which generally exist at frequencies higher than the unstable Class A TSI waves at the same R_δ, are suppressed by the appropriate level of material damping in the third

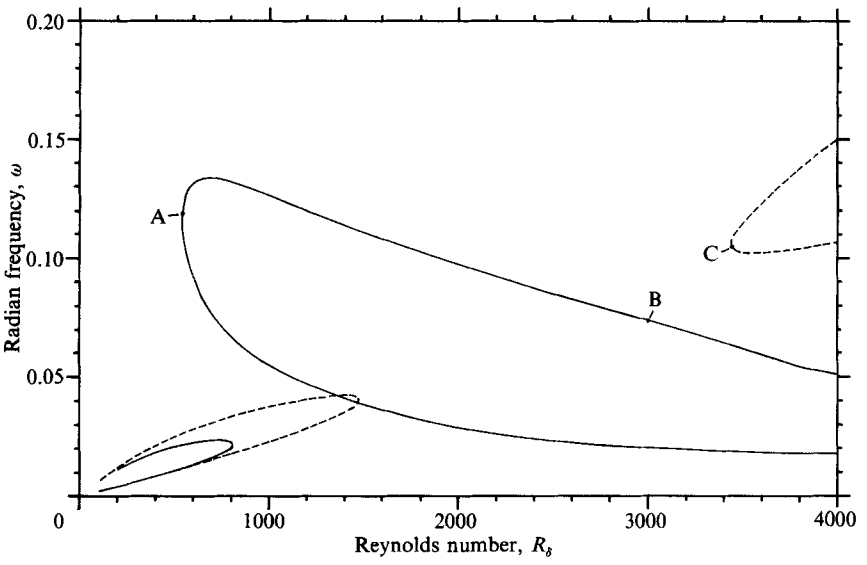

FIGURE 22. The marginal stability curves for a multi-layer wall.

Material data for: ——

Layer no.	h	C_t	d	K
1	0.5	2.0	0.0049	500
2	1.5	0.8	0.0049	500
3	1.0	0.4	0.0294	0.267
4	0.5	0.8	0.0049	500

Material data for: – – – – –

As above except third-layer $d = 0.01225$.

layer. The shorter-wavelength and higher-frequency TSI will be somewhat destabilized by the described configuration but these do not matter as much as the longer-wavelength TSI waves insofar as transition is concerned.

Figure 22 shows the marginal stability curves for one of the four-layer walls. The effects of material damping in the third layer on the CIFI is depicted. For $d^{(3)} = 0.01225$, the unstable B_1 regime has a R_δ^{cr} of around 3440 (corresponding A regime not shown for clarity). At $d^{(3)} = 0.0294$, the unstable B_1 regime retreats way beyond $R_\delta = 4000$. The unstable TSI regime which is shown has a critical Reynolds number R_δ^{cr} of 542.85, very slightly larger than the rigid-wall value. The relatively low value of the critical Reynolds number R_δ^{cr} is largely a consequence of the stiff resistance encountered by the shorter wavelength TS disturbances in the top layer. Comparison with the rigid-wall marginal stability curve reveals the rapid reduction in the ω-bandwidth with increasing R_δ. The local amplification rates at large R_δ are thus substantially less than those for the rigid wall. Further improvement of the A or TSI regime is achieved when the top-layer $C_t^{(1)}$ is reduced to 1.0. The marginal curves are shown in figure 23 together with the marginal curve of the rigid wall. The reduction in $C_t^{(1)}$ produces a new R_δ^{cr} of 643.89 together with further decrease in the ω-bandwidth from the previous case ($C_t^{(1)} = 2.0$) over much of the Reynolds-number range. The upper neutral boundaries for the two compliant cases converge as we get to higher R_δ beyond 4000. Comparison with the rigid-wall neutral boundary clearly illustrates the extent of the improvement for the TSI regimes. The local amplification rate contours for $\alpha_i = -0.0015$ and -0.003 are also shown. At $R_\delta = 4000$, the

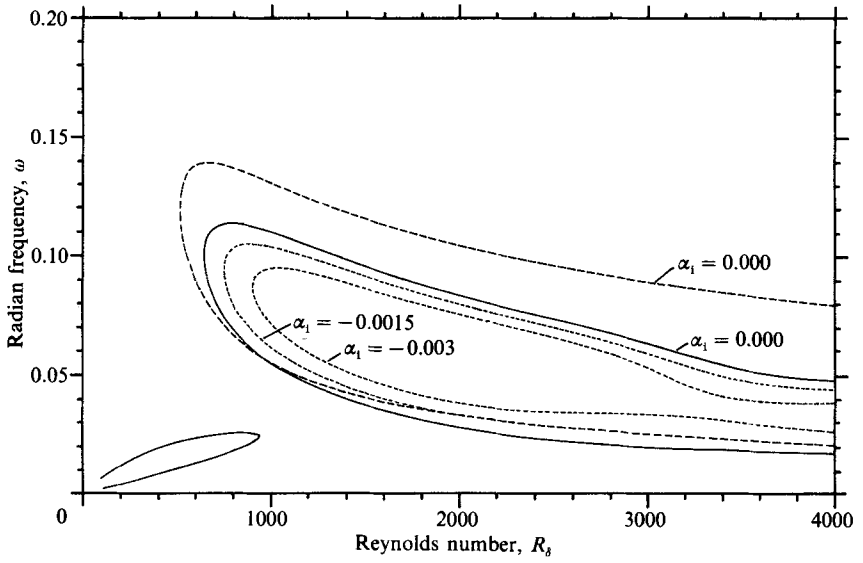

FIGURE 23. Curves of constant α_i for a multi-layer wall.

Material data for compliant wall:

Layer no.	h	C_t	d	K
1	0.5	1.0	0.0049	500
2	1.5	0.8	0.0049	500
3	1.0	0.4	0.0294	0.267
4	0.5	0.8	0.0049	500

------, ——, compliant wall; ———, rigid wall.

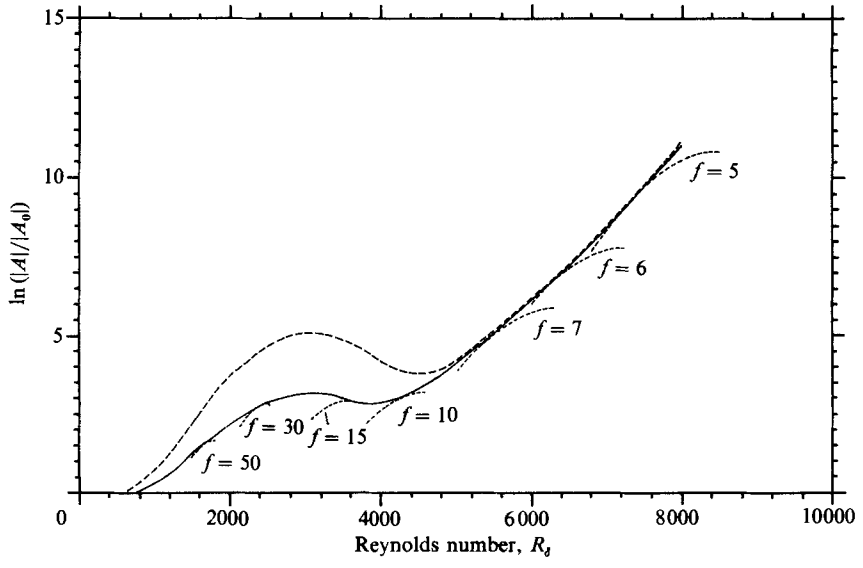

FIGURE 24. The maximum amplification envelopes for two four-layer walls. ———, four-layer wall of figure 22; ——, four-layer wall of figure 23; ------, total amplification curves at $F = f \times 10^{-6}$.

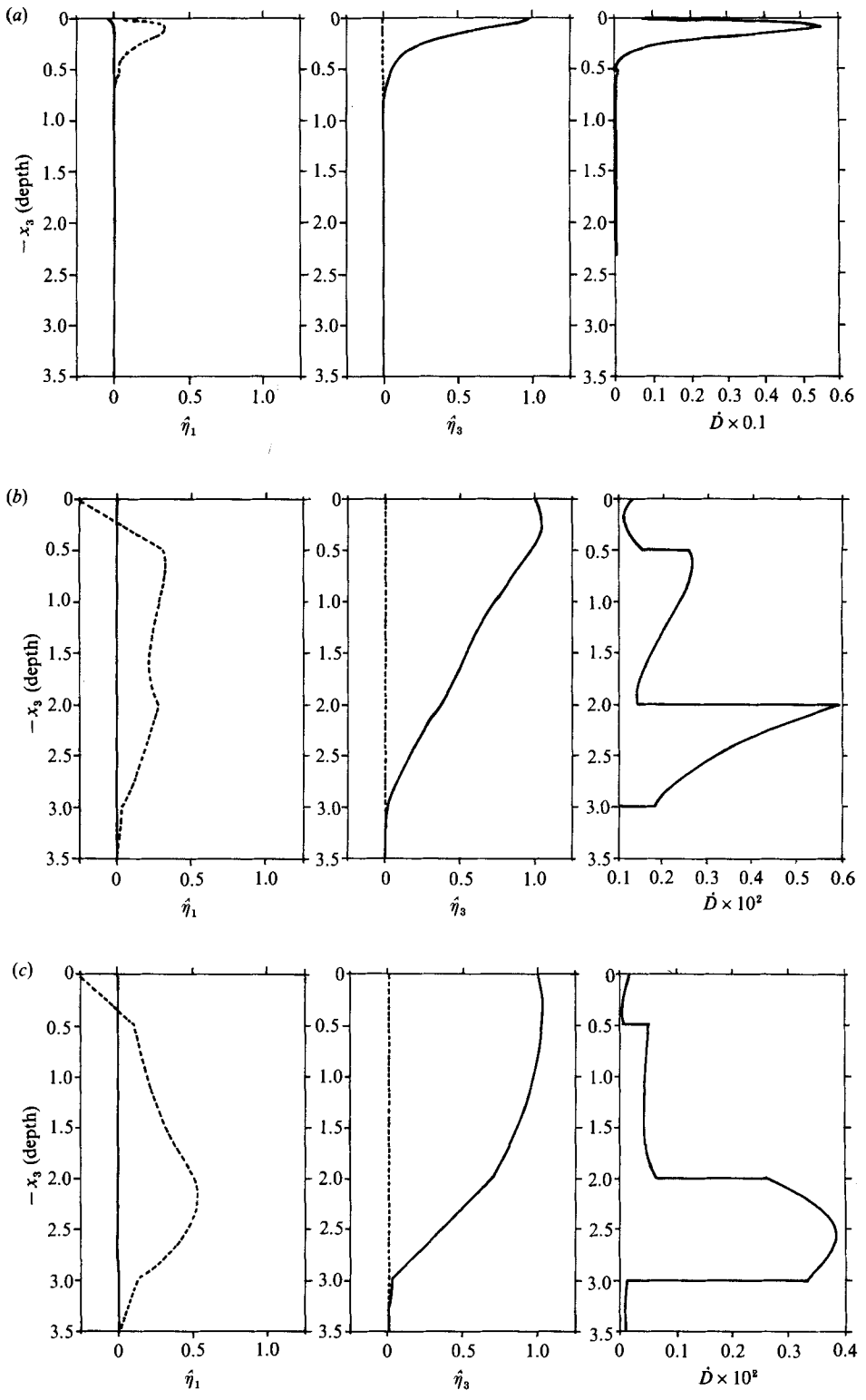

FIGURE 25. Wall eigenfunctions for eigenstates of the four-layer walls of figure 22. (*a*) Eigenstate A. (*b*) Eigenstate B. (*c*) Eigenstate C. ——, real part; ------, imaginary part.

Layer no.	Thickness (mm)	Young's modulus (N/mm^2)
1	0.5556	0.972
2	1.6667	0.622
3	1.1111	0.156
4	0.5556	0.622

TABLE 1

maximum local amplification rate is slightly less than 30% of the rigid-wall maximum. The total amplification envelopes for the two four-layer walls are given in figure 24. A maximum spatial amplification factor of $e^{8.3}$ is achieved by the two walls at $R_x \approx 16.27 \times 10^6$ ($R_\delta \approx 6940$) for the case with $C_t^{(1)} = 1.0$ and $R_x \approx 16.17 \times 10^6$ ($R_\delta \approx 6920$) for $C_t^{(1)} = 2.0$. These results represent substantial delay in transition provided the $e^{8.3}$ transition rule holds. It is important to be reminded that these results are for two-dimensional disturbances. Reduced streamwise transition distances are predicted when oblique wave modes are taken into account; Yeo (1986).

The eigenfunctions at three neutral eigenstates denoted A, B and C in figure 22 are shown in figure 25. The displacement eigenfunctions in figure 25(*b*) for the eigenstate on the upper neutral branch of the TSI regime indicate plate-like response in the top layer. A good deal of the dissipation of disturbance energy within the wall occurs in the soft and highly compressible third layer. For the eigenstate at the nose of the A regime, denoted A in figure 22, the streamwise wavelength of the disturbance is approximately 0.58, only slightly larger than the thickness of the first layer ($h^{(1)} = 0.5$). Because this wavelength is only of the order of the thickness of the top layer, the top layer no longer behaves like a plate, but instead, merely resists the penetration of the disturbance wave by its sheer stiffness (figure 25*a*). This results in a very sharp decline of the disturbance amplitude within the first layer. In figure 25(*c*), we have the eigenfunctions for the eigenstate at the nose of the B_1 regime for $d^{(3)} = 0.012\,25$. There is a plate-like response from the top layer. Again it is observed that most of the dissipation of disturbance energy within the wall occurs in the third layer. Variation of the material damping coefficient d here has a strong influence on the CIFI. The third layer corresponds precisely to Kramer's layer of stubs and viscous damping fluid.

If we assume a free-stream velocity of 18 m/s, a density of 10^3 kg/m^3 and a kinematic viscosity of 10^{-6} m^2/s for the flow, the dimensions and properties of the four-layer wall given in figure 23 work out as in table 1. The overall thickness of the wall is 3.889 mm and the above Young's moduli are elastic Young's moduli based only on the elastic shear speed C_t. It is remarkable that these thicknesses and Young's moduli are of the same order as those quoted by Carpenter & Garrad (1985) for the best of the Kramer's original walls.

The two walls considered in this section exhibited potential transition distances in excess of 5.6 times the transition distance found on rigid walls. They are of similar order to, but less than, the maximum transition delay distances obtained by Gyorgyfalvy (1967) for similar flow over spring-backed membrane with viscous damping, and are higher than those implied in table 3 of Carpenter & Garrad (1985) for the best Kramer-type walls. Gyorgyfalvy's results were based primarily on the growth of the TSI waves. However, it is not clear from his paper what criteria he had employed in discounting the Class B and Class C instabilities.

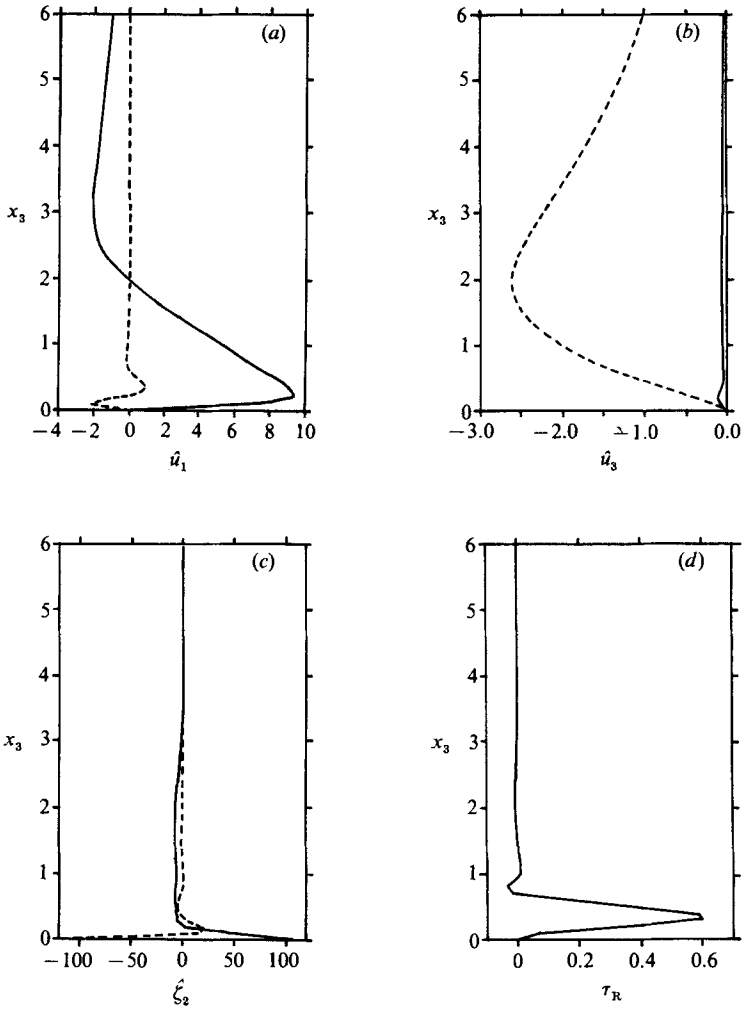

FIGURE 26. Flow eigenfunctions on the upper neutral curve at $R_\delta = 4000$ for the rigid wall. (*a*) $\hat{u}_1$, (*b*) $\hat{u}_3$, (*c*) $\hat{\zeta}_2$, (*d*) τ_R. ——, real part; ------, imaginary part.

6. Flow eigenfunction and stability

In the preceding sections, the study of wall eigenfunctions provides valuable insight into some of the mechanics underlying the predicted stability behaviour. Some analyses of flow eigenfunctions were also made and the more salient points are noted below together with observations concerning their relation to flow stability.

Figures 26 and 27 show the various flow eigenfunctions for the neutral eigenstates on the upper neutral boundary of the TSI regime at $R_\delta = 4000$ for a rigid wall and the four-layer compliant wall of figure 23 respectively. These eigenfunctions have been normalized in such a manner that $\overline{(u_j)_r (u_j)_r}$, termed the mean perturbation kinetic energy density, is 1.0 at $x_3 = 6$ (displacement thicknesses) and the argument of $\hat{u}_{1,3}$, $\mathrm{Arg}(\hat{u}_{1,3}) = -\frac{1}{4}\pi$ at $x_3 = 0$. The perturbation velocity components at the mean position of the wall at $x_3 = 0$ are non-zero for the compliant wall. This is to be expected because of the interface boundary conditions they must satisfy. It will also be observed that the Reynolds stress (τ_R) distribution for the compliant wall

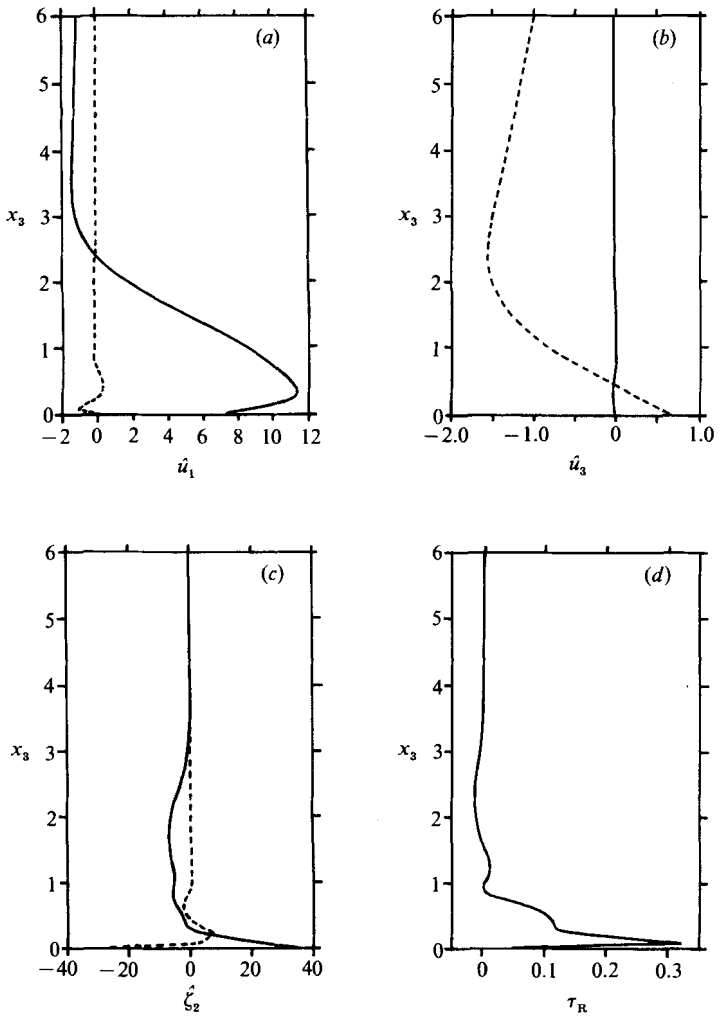

FIGURE 27. Flow eigenfunctions on the upper neutral curve of the A regime at $R_\delta = 4000$ for the compliant wall of figure 23. (*a*) $\hat{u}_1$, (*b*) $\hat{u}_3$, (*c*) $\hat{\zeta}_2$, (*d*) τ_R. ——, real part; ------, imaginary part.

eigenstate is significantly lower than that for the rigid wall. This means that, subject to the normalization, the total rate of energy transfer from the basic flow to the disturbance is lower in the case of the compliant wall. Since the disturbance is neutrally stable, this is also equal to the rate at which the disturbance energy is being dissipated within the flow and the wall. The reduced total dissipation rate of the system and its improved stability over the rigid-wall case are consistent with the Class A nature of the Tollmien–Schlichting instability. The distributions of disturbance vorticity amplitude $\hat{\zeta}_2$, where $\zeta_2 = u_{1,3} - u_{3,1}$, are also shown for the two walls. The level of disturbance vorticity over the compliant wall is clearly much lower than that over the rigid wall, showing that compliant wall stabilization may also be associated with greatly reduced levels of disturbance vorticity ζ_2 in the flow. The maximum of $|\hat{\zeta}_2|$ for the compliant wall eigenstate is about $\frac{1}{3}$ that of the rigid-wall eigenstate; the maximum moduli occur at $x_3 = 0$ in both cases. The above typically holds for other eigenstates on the upper neutral branch of the TSI loop when

stabilization is observed; the stronger the stabilizing influence of the compliant wall the more pronounced are the noted effects.

For a compliant wall, the total flux of disturbance vorticity ζ_2 across the mean interface per unit area and time is given by

$$-\frac{1}{R}\zeta_{2,3}+u_3 U_{,3}. \tag{6.1}$$

This may be deduced from the conservation form of the linearized disturbance vorticity equation. The first term represents a diffusive flux of ζ_2. This is generated in response to the propagating disturbance field in the near-wall region so as to maintain at all times the non-slip flow condition required by the presence of viscosity. The second term $u_3 U_{,3}$ represents the convective transport of mean flow vorticity across $x_3 = 0$ induced by the wave motion on the compliant boundary. The underlying mechanics of the transport may be said to be inertial because it could theoretically exist even in the absence of viscosity provided $U_{,3}$ is not zero at $x_3 = 0$. While the mechanics of the transport is determined by inertial factors, the existence of non-zero mean flow vorticity $U_{,3}$ is in reality a consequence of the non-slip condition $U_3|_{z_0} = 0$ imposed by viscosity on the mean flow. Thus $u_3 U_{,3}$ really represents a convective transport of viscosity-generated vorticity induced by inertial factors. In the case of a rigid boundary, the convective flux is absent, and it is the outward diffusion of the viscosity-generated flux $-\zeta_{2,3}/R_\delta$ and its constructive interference with the oncoming disturbance vorticity in the near-wall region that constitute the physical basis of Tollmien–Schlichting instability over rigid surfaces; see §3 of Lighthill (1963). For TS waves over compliant surfaces, however, the stability is determined by the total flux (6.1) rather than the diffusive flux alone.

For the compliant wall eigenstate given in figure 27, the viscosity-generated flux $-\zeta_{2,3}/R_\delta$ is only about $\frac{1}{3}$ that for the corresponding rigid wall eigenstate (figure 26). Hence, subject to the normalization, compliant wall response is seen to have reduced the rate at which disturbance vorticity is being produced at the wall via viscosity. This accords very well with the cancelling effect of compliant wall motion on the wall friction layer mentioned by Benjamin (1964). In addition, calculation shows that the amplitude modulus $|\hat{u}_3 U_{,3}|$ is about 2.35 times that of $|\hat{\zeta}_{2,3}|/R_\delta$ at $x_3 = 0$. The phase difference between the two fluxes is about 175° and hence indicates a substantial cancellation of the diffusive flux. Thus we see that the stabilization of the TS mode is also associated with a process in which the viscosity-generated vorticity of the mean flow is directed by the appropriate wall motion to produce a cancelling effect on the component of viscosity-generated diffusive flux. For this compliant wall eigenstate, the total outward flux of disturbance vorticity ζ_2 is dominated by inertial contributions and the phase of ζ_2 is determined largely by the wave motion of the surface. It is also noted that, in general, the dominance of the inertial flux increases with the degree of stabilization obtained.

In the case of CIFI, $u_3 U_{,3}$ is generally found to be much more dominant than $-\zeta_{2,3}/R_\delta$ over much of the flow domain. This is because the mechanics of CIFI is largely determined by inertial effects. Except at low Reynolds numbers, viscosity plays a comparatively minor role in CIFI.

7. Conclusions

The linear stability of boundary-layer flow over single and multi-layer walls to two-dimensional disturbance modes was studied. The response of a multi-layer wall was given a simple representation using a displacement-stress vector formulation. The formulation permits a systematic numerical implementation of the eigenvalue problem which is applicable to walls having any finite number of layers. Furthermore, the treatment extends naturally to anisotropic-material walls as well as three-dimensional wave propagation in multi-layer walls, see Yeo (1986). The present model also takes into account the coupling of shear stress perturbation at the flow–wall interface which is omitted in almost all previous studies.

The effects wall compliance and wall damping have on the various instability modes were found to be generally consistent with the results of earlier works. A long-wavelength instability (relative to local displacement thickness) which persists to very low Reynolds numbers was also found. This instability, termed B_2 in the present work, generally has small spatial growth rates and is believed not to be important as far as transition is concerned. It is a CIFI and may be related to the low-Reynolds-number instability modes noted in Landahl (1962).

To have significant effect on stability, the material C_t for a single-layer wall needs to be less than the free-stream velocity. When C_t is near to 1.0, the CIFI are not important and may be suppressed with a small amount of material damping. However, the gain in the stability for the TSI regime is also modest. For a softer material with $C_t = 0.7$, the CIFI become important, but these may be effectively suppressed by increasing wall damping, resulting in a significant net gain in overall stability. Provided it is possible to suppress the CIFI by increasing the material damping, thicker wall layers are preferable to thinner ones because they sustain lower spatial amplification rates for the Class A TSI waves at the larger R_δ. This is because damping has a mild destabilizing influence on the lower frequency TSI waves which exist at larger R_δ. In such cases, substantial delay of transition was found to be theoretically possible accordingly to a $e^{8.3}$ transition rule because of greatly reduced local amplification rates. High levels of damping may, however, also lead to significant reduction in the critical Reynolds number R_δ^{cr} of the A or TSI regimes. The stability eigenvalue spectra for single-layer walls with low C_t, such as 0.5, was found to be highly complex. In places, it was virtually impossible to determine the spatial stability eigenstates because of what appears to be branch-cut behaviour associated with the continuous spectra in the α-plane. Our results for these are incomplete, but what appears to be fairly certain is that there are strong CIFI which cannot be effectively suppressed by material damping alone. Coalescence between unstable TSI and CIFI was also noted. Reduction in the Bulk modulus (or increase in material compressibility) stabilizes the TSI and destabilizes the CIFI. The effect is, however, significant only when c_L reaches the order of C_t.

The study of wall eigenfunctions shows that the magnitude of $(\alpha_w)_r$ (real wavenumber in wall lengthscale) is a good indicator of the penetrative quality of a disturbance mode. Disturbance waves having high $(\alpha_w)_r$ (short wavelength) tend to persist in a thin layer near the surface whereas waves with small $(\alpha_w)_r$ permeate the entire layer. The frequency of a disturbance mode also determines its response to an increase in the wall damping coefficient d. When the frequency ω is low (high), the effect on the stability of the mode from an increase in d is correspondingly small (large). This may be related to the use of the Voigt model, in which the loss tangent (a measure of the 'quality' of damping) is proportional to ω_w.

In the case of two-layer walls, the thin top layers were found to assume a very distinctive plate-like behaviour when they are materially much stiffer than the second thick layer. In such cases, some of the effects of the properties and the thickness of the top thin layer on flow stability may be qualitatively explained on the basis of the plate-like response. A thin top plate-like layer with greater resistance to bending tends to stabilize the CIFI and destabilize the TSI. For top plate-like layers having unit density and the same flexural rigidity, a thinner layer with higher C_t was found to be preferable to a thicker layer with lower C_t because of its strong stabilizing influence on the CIFI and small destabilizing influence on the TSI.

A thin stiff layer clearly has a very strong stabilizing influence on the CIFI when it is placed at a short distance below the surface of the softer layer. Placing a thin layer in an embedded position tends to destabilize the A or TSI regime but such an effect appears to be small at the higher R_δ. Thus, careful positioning of a thin stiff layer in an embedded position near the surface appears to be a promising way to obtain an overall gain in stability.

A specific class of four-layer walls bearing some geometric similarities with the original Kramer walls was studied. Based largely upon the understanding gained from the studies of single-layer and multi-layer walls, the material properties of the layers were selected to give good stability performance from the point of view of effective suppression of the CIFI and low spatial amplification rates for the TSI. Results for two specific walls were presented which exhibit good transition delaying potential and these remarkably have material moduli which are of similar order to those quoted by Carpenter & Garrad (1985) for the best Kramer walls. The role of damping in the third and highly compliant layer, which corresponds to the layer of stubs in the Kramer walls, was crucial to the inhibition of the CIFI. This suggests that the viscous substrates in Kramer's better walls might have served the same function.

The disturbance vorticity flux from the boundary may be decomposed into a viscosity-induced diffusive flux and a convective flux. For stabilized TS waves reduction in the diffusive flux is noted. This accords with the friction-layer cancellation effect suggested by Benjamin (1964). Compliant wall motion also induces a convective transfer of mean flow vorticity across the mean flow–wall interface. The stabilization of the Tollmien–Schlichting wave mode is also observed to be associated with a process in which mean flow vorticity is directed by the wall motion to produce a cancellation effect on the diffusive flux of disturbance vorticity produced by viscosity at a solid surface. At the higher Reynolds numbers the stabilized TS modes are also observed to have

(*a*) a convection-dominated flux of disturbance vorticity ζ_2 at $x_3 = 0$ and,

(*b*) subject to the normalization used, greatly reduced levels of disturbance vorticity ζ_2 and Reynolds stresses in the flow.

Except at low Reynolds numbers, the convective flux of ζ_2 dominates over the diffusive flux in the case of CIFI modes.

The author wishes to thank Dr Ann P. Dowling for the invaluable guidance and encouragement she has given him during the course of this work. The author also benefited greatly from the various discussions he had with Professor M. Gaster to whom he would like to register his greatest appreciation herein. The main part of this work was done while the author was on study leave at the University of Cambridge. The financial support of the National University of Singapore and the Commonwealth Trust Fund is gratefully acknowledged.

REFERENCES

BENJAMIN, T. B. 1960 Effects of a flexible boundary on hydrodynamic stability. *J. Fluid Mech.* **9**, 513.

BENJAMIN, T. B. 1963 The three-fold classification of unstable disturbances in flexible surfaces bounding inviscid flows. *J. Fluid Mech.* **16**, 436.

BENJAMIN, T. B. 1964 Fluid flow with flexible boundaries. In *Proc. 11th Intl Congr. Appl. Mech., Munich, Germany*, p. 109.

BERS, A. & BRIGGS, R. J. 1964 *Bull. Am. Phys. Soc.* **9**, 304.

BLAND, D. R. 1960 *Linear Viscoelasticity.* Pergamon.

CARPENTER, P. W. & GARRAD, A. D. 1985 The hydrodynamic stability of flow over Kramer-type compliant surfaces. Part 1. Tollmien–Schlichting instabilities. *J. Fluid Mech.* **155**, 465.

CARPENTER, P. W. & GARRAD, A. D. 1986 The hydrodynamic stability of flow over Kramer-type compliant surfaces. Part 2. Flow-induced surface instabilities. *J. Fluid Mech.* **170**, 199.

CARPENTER, P. W., GASTER, M. & WILLIS, G. J. K. 1983 A numerical investigation into boundary layer stability on compliant surfaces. In *Numer. Meth. Lam. Turb. Flows, Swansea*, p. 165.

CHUNG, K. H. & MERRILL, E. W. 1984 Drag reduction by compliant surfaces measured on rotating discs. Abstract submitted to the Compliant Coating Drag Reduction Prog. Rev., Off. Naval Res.

CRAIK, A. D. D. 1966 Wind-generated waves in thin liquid films. *J. Fluid Mech.* **26**, 369.

DAVEY, A. 1981 A difficult calculation concerning the stability of Blasius boundary layer. *Proc. IUTAM Symp. on Stability in Mech. of continua, Numbrecht, Germany*, p. 365.

DRAZIN, P. G. & REID, W. H. 1981 *Hydrodynamic Stability.* Cambridge University Press.

FRASER, L. A. 1984 The hydrodynamic stability of flows over homogeneous elastic layers. Presented at *Euromech Colloquium 188, 23–26 Sept. 84*, University of Leeds, England.

FRASER, L. A. & CARPENTER, P. W. 1985 A numerical investigation of hydroelastic and hydrodynamic instabilities in laminar flows over compliant surfaces comprising of one or two layers of viscoelastic materials. In *Numerical Methods in Laminar and Turbulent Flows*, p. 1171. Pineridge.

GASTER, M. 1962 A note on the relation between temporally-increasing and spatially-increasing disturbances in hydrodynamic stability. *J. Fluid Mech.* **14**, 222.

GASTER, M. 1965 On the generation of spatially growing waves in a boundary layer. *J. Fluid Mech.* **22**, 433.

GASTER, M. 1974 On the effects of boundary layer growth on flow stability. *J. Fluid Mech.* **66**, 465.

GASTER, M. 1984 Stability of laminar boundary layers on compliant boundaries: Theory and experiments at NMI Ltd. Abstract submitted to the Compliant Coating Drag Reduction Prog. Rev., Off. Naval Res.

GASTER, M. 1985 Growth of instability waves over compliant coatings. *Bull. Am. Phys. Soc.* **30**, 1708.

GASTER, M. 1987 Is the dolphin a red herring. *Proc. IUTAM Symp. on Turbulence Management and Laminarization, Bangalore, India*, p. 285.

GILBERT, F. & BACKUS, G. E. 1966 Propagation matrices in elastic wave and vibration problems. *Geophysics* **31**, 326.

GYORGYFALVY, D. 1967 Possibilities of drag reduction by the use of flexible skin. *J. Aircraft* **4**, 186.

JAFFE, N. A., OKAMURA, T. T. & SMITH, A. M. O. 1970 Determination of spatial amplification factors and their application to predicting transition. *AIAA J.* **8**, 301.

JORDINSON, R. 1970 The flat plate boundary layer. Part 1. Numerical integration of the Orr–Sommerfeld equation. *J. Fluid Mech.* **43**, 801.

KAPLAN, R. E. 1964 The stability of laminar boundary layers in the presence of compliant boundaries. ScD thesis, MIT.

KRAMER, M. O. 1957 Boundary-layer stabilization by distributed damping. *J. Aero Sci.* **24**, 459.

KRAMER, M. O. 1960 Boundary layer stabilization by distributed damping. *J. Am. Soc. Naval Engng* **73**, 25.

LANDAHL, M. T. 1962 On the stability of a laminar incompressible boundary layer over a flexible surface. *J. Fluid Mech.* **13**, 609.

LANDAHL, M. T. & KAPLAN, R. E. 1965 Effect of compliant walls on boundary layer stability and transition. *AGARDograph* **97**, 363.

LIGHTHILL, M. J. 1963 Boundary layer theory. In *Laminar Boundary Layer* (ed. L. Rosenhead). Oxford University Press.

NG, B. S. & REID, W. H. 1979 An initial-value method for eigenvalue problems using compound matrices. *J. Comp. Phys.* **30**, 125.

NONWEILER, T. 1963 Qualitative solutions of the stability equation for a boundary layer in contact with various forms of flexible surface. *Aeronaut. Res. Council Rep.* CP622.

SCHUBAUER, G. B. & SKRAMSTAD, H. K. 1948 Laminar boundary-layer oscillations and transition on a flat plate. *NACA Rep.* 909.

SMITH, A. M. O. & GAMBERONI, H. 1956 Transition, pressure gradient and stability theory. *Douglas Aircraft Co., Long Beach, Calif., Rep.* ES26388.

THOMSON, W. T. 1950 Transmission of elastic waves through a stratified solid medium. *J. Appl. Phys.* **21**, 89.

WELLS, C. S. 1967 Effects of freestream turbulence on boundary-layer transition. *AIAA J.* **5**, 172.

WILLIS, G. J. K. 1987 Hydrodynamic stability of boundary layers over compliant surfaces. PhD thesis, University of Exeter.

YEO, K. S. 1986 The stability of flow over flexible surfaces. PhD thesis, University of Cambridge.

YEO, K. S. & DOWLING, A. P. 1987 The stability of inviscid flows over passive compliant walls. *J. Fluid Mech.* **183**, 265.